

## Review

## Energy absorption of origami inspired structures and materials

X.M. Xiang<sup>a</sup>, G. Lu<sup>b,\*</sup>, Z. You<sup>c, \*\*</sup><sup>a</sup> School of Civil Engineering, Guangzhou University, Guangzhou Panyu University City, Outer Ring Road No. 230, Guangzhou, 510006, China<sup>b</sup> Faculty of Science, Engineering and Technology, Swinburne University of Technology, Hawthorn, Vic, 3122, Australia<sup>c</sup> Department of Engineering Science, University of Oxford, Parks Road, Oxford, OX1 3PJ, UK

## ARTICLE INFO

## Keywords:

Origami pattern  
Energy absorption  
Deformation process  
Failure mode

## ABSTRACT

Origami structures are commonly constructed by folding a two-dimensional sheet according to a given crease pattern. The existence of abundant crease patterns means that many three-dimensional structures can be fabricated by using a variety of sheet materials, including thin-walled tubes and arcs. Some origami structures can also be used as core structures, sandwich plates, or arcs, whereas other such structures can be stacked to form metamaterials, which are materials designed to possess a property that is not readily available in nature. Because the mechanical performances of these structures are commonly dependent upon their geometry, the properties of these structures can be designed and adjusted through the selection and optimization of the appropriate geometric parameters. This review focuses on the deformation and energy absorption (EA) capability of origami structures subjected to static and dynamic loading. The main characteristics and findings are summarized, and further work in the area is suggested.

## 1. Introduction

The word *origami* refers to an ancient art of paper folding, and it contains two Japanese roots: *ori* and *kami*, meaning ‘folded’ and ‘paper,’ respectively [1]. Since the beginning of the twentieth century, origami has become a popular recreational activity around the world [2], and in the recent decades, origami has been of increasing interest to many engineers. Researchers have noted that the traditional geometry and folding used for artistic paper models can be readily parameterized and applied to the development of new structures and devices. Origami that permits the realization of continuous motion between the folded states along the predetermined folding creases enables structures to be readily manufactured from modern materials such as plastic, metal, or carbon fiber sheets and helps produce structures that are sufficiently strong and durable to be of use in large-scale applications [3,4].

Some terms commonly used in origami are introduced as follows [5]: (1) crease: a fold line, either convex (mountain, represented by solid lines in this work) or concave (valley, represented by dashed lines); all the creases making up the crease pattern; (2) vertex: a point where the creases intersect; (3) the folded state: the end state of the folding motion. To construct an origami structure, the first step is to design a crease pattern. Fig. 1 shows several of the most commonly used crease patterns

for engineering applications: the waterbomb, Miura-ori [6], Yoshimura and diagonal patterns, as well as the structures folded according to these patterns. These patterns are known as tessellation origami patterns, in which the same unit is repeated over the entire sheet. The structures based on the waterbomb and the Miura-ori pattern expand and contract in all the directions while those obtained from the Yoshimura and diagonal patterns only allow for translational and rotational motions [5].

If a pattern can be folded purely by the rotation of faces around the creases, the pattern corresponds to rigid origami, in which each face is considered as a rigid body and the origami structure is an assembly of the rigid faces connected by line hinges [7]. The motions of a rigid origami structure can be modeled kinematically by treating the creases as perfect line hinges. Origami-inspired structures have been used in medical, aerospace, mechanical and civil engineering applications primarily owing to their foldability. For example, some origami structures become extremely compact while folded, making them ideal for use in deployable shelters and space solar panels [8,9]. However, in this review, we focus on the family of origami structures that are not created for their foldability. Instead, these structures are related to origami simply because origami makes it possible to fabricate these structures out of flat sheet materials. These structures are generally manufactured from sheet materials and later rigidized once the required shapes or

\* Corresponding author.

\*\* Corresponding author.

E-mail addresses: [glu@swin.edu.au](mailto:glu@swin.edu.au) (G. Lu), [zhong.you@eng.ox.ac.uk](mailto:zhong.you@eng.ox.ac.uk) (Z. You).

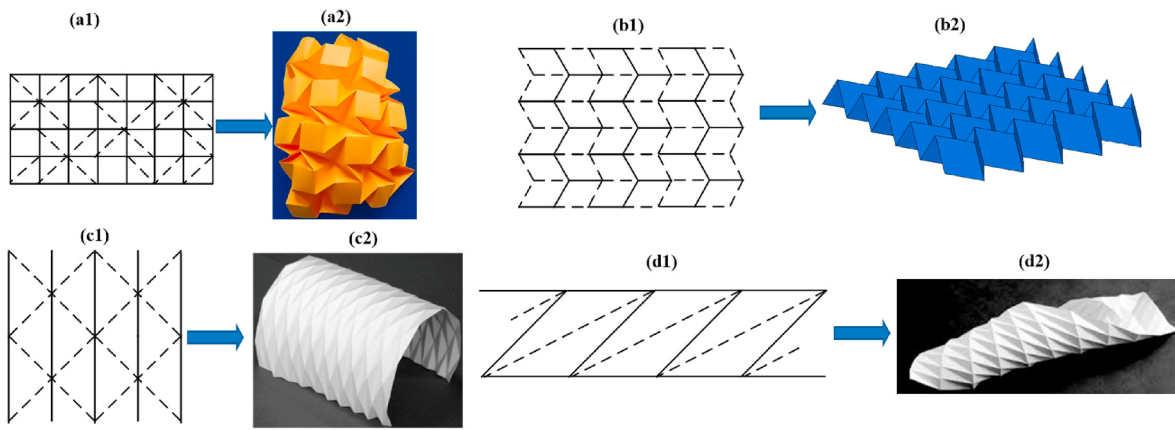


**Fig. 1.** Typical origami crease patterns and folded structures. (a1-a2) The waterbomb crease pattern and folded structure [7]; (b1-b2) the Miura-ori crease pattern and folded structure [15]; (c1-c2) the Yoshimura crease pattern and folded structure [15]; (d1-d2) the diagonal crease pattern and folded structure [15]. Solid lines indicate mountains, while dashed lines indicate valleys.

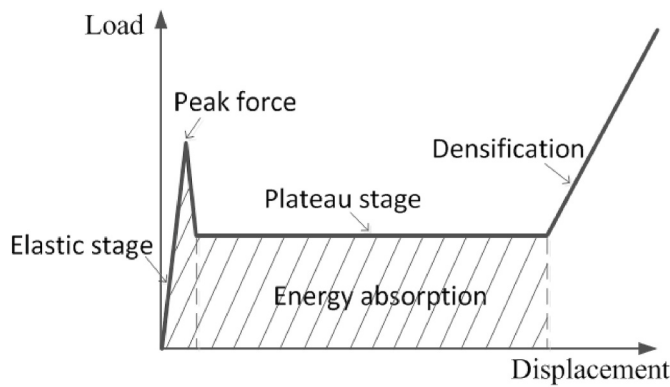


**Fig. 2.** Idealized load-displacement relationship of the energy absorbing materials and structures. The area under the curve represents the energy absorbed.

profiles are formed. The structure geometry and existence of creases in these structures enable these structures to have exceptional mechanical performances, such as tunable stiffness [10], negative Poisson's ratio [11], tunable acoustic [12] and thermal [13] properties and favorable failure modes that provide a higher energy absorption (EA) capability when subjected to impact [14]. This review is focused on the EA capability of the origami structures under impact.

The EA performance is an important mechanical property of structures, which is commonly evaluated by analyzing the displacement vs. load plot of a structure subjected to impact loading, such as the one presented in Fig. 2. An ideal energy absorbing structure should meet the following requirements [16]:

- Irreversible energy conversion to avoid a second impact caused by the energy switch.
- Long stroke to allow space for plastic deformation.
- Stable and predictable performance in each impact.
- Restricted and constant reactive force to ensure that no excessive force is transmitted to the main structure to be protected.
- Light weight and high EA to absorb as much energy as possible, which is commonly quantified using the specific energy absorption (SEA), defined as the energy absorbed per unit mass. The SEA is usually employed as a key performance parameter. In addition, it is desirable for the load-displacement curve to have a low peak force and a plateau force over a long stroke of displacement.
- Satisfactory load uniformity, defined as the ratio of the peak force to the mean crushing force ( $F_m$ ).

- Low cost and easy installation as the structure is a one-shot device and needs replacement after an impact accident.

Metallic thin-walled structures dissipate energy by large plastic bending along the idealized hinge lines, possibly coupled with in-plane stretching or compression. The deformation modes and mechanisms, represented by the stationary or traveling hinge lines and geometrical patterns, are formed naturally during the plastic deformation. It is often postulated that the shape and values of the geometric parameters describing the deformation modes are such that the minimum corresponding total energy is dissipated [17]. Origami offers a simple and innovative route for the design of energy absorbing structures. Research has shown that by merely introducing one or several initial folds into a structure, the deformation modes can be changed because the initial creases act as engineered imperfections. Some of these deformation modes, partially prescribed *a priori*, are associated with considerably higher EA than that of their conventional structural counterparts during plastic deformation. In addition, the initial folds can also be used to adjust the peak force and even the complete force-displacement characteristics.

In this paper, we try to provide an overview of the EA of origami structures subjected to either quasi-static or dynamic load, describe the current status and explore future directions in this emerging research area. The layout of the review is as follows. In Section 2, we consider the thin-walled tubular origami structures under axial and lateral loads. In Section 3, we review the origami plate structures, including foldcores and sandwich plates formed by adding top and bottom skins to the foldcores. This review is followed by that of the origami arcs in Section 4. A new family of origami metamaterials is discussed in Section 5. Finally, a few suggestions for future research are provided in Section 6.

## 2. Origami thin-walled tubes

A low peak force and long plateau force with small fluctuations are highly favorable features of the energy absorbing structures. When used as energy absorbers, the large initial peak force ( $F_{max}$ ), the force fluctuation and the very low  $F_m$  are the main disadvantages of conventional thin-walled tubes. In recent years, engineers have attempted to use origami folds to minimize the initial peak and subsequent fluctuation for thin-walled tubes. The first such adoption is a Miura-ori cylinder crash box reported by Nojima [18]. The other relevant origami structure is a beverage can concept consisting of a diamond pattern. Instead of achieving a higher EA, the latter design aims to facilitate the crushing of an empty can for recycling [19]. In both designs, in addition to the origami pattern itself, the number of modules along the axial direction ( $M$ ) (shown in Fig. 3 (a)) and the dihedral angle ( $\theta$ ) between the two

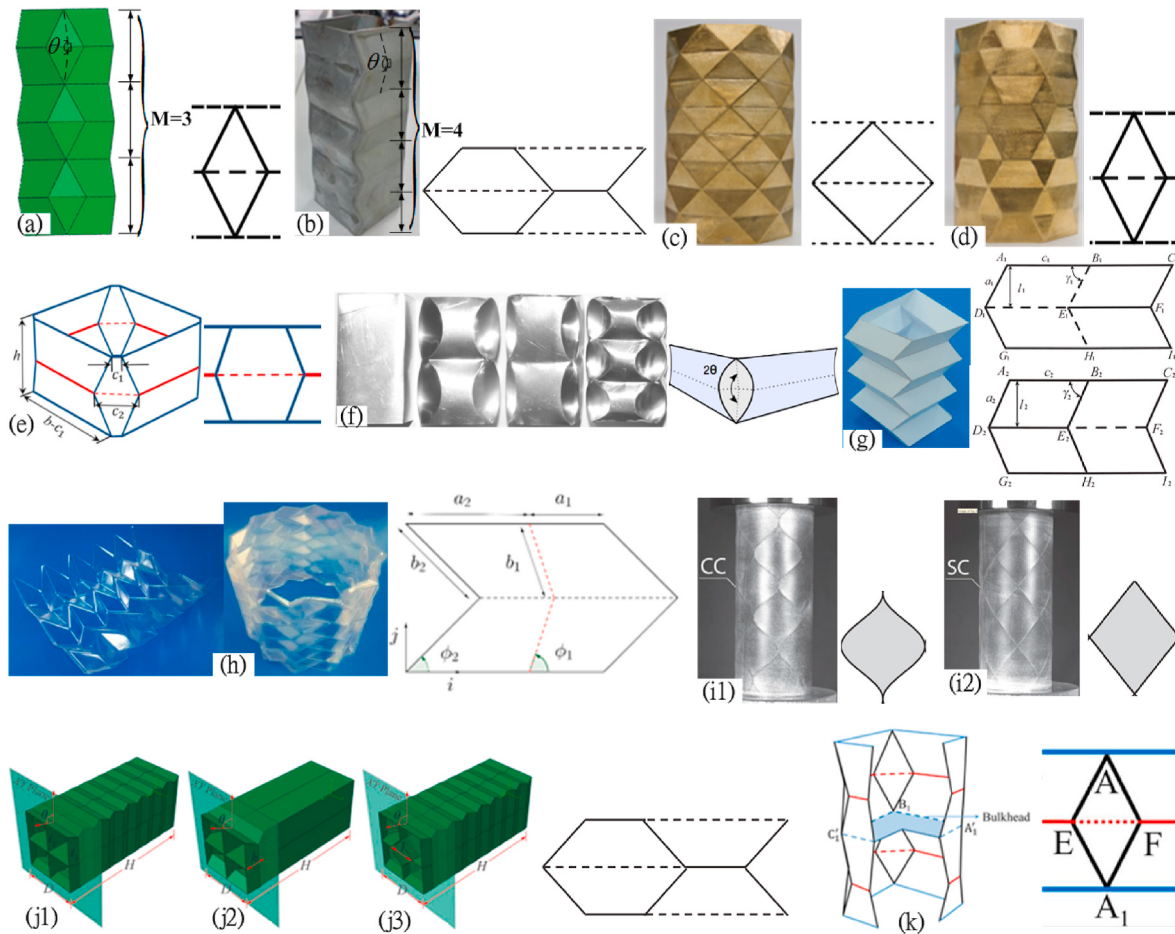


**Fig. 3.** Various origami tubes and the corresponding crease patterns. (a) Diamond origami crash box [21]; (b) prefolded origami tube [20]; (c) full diamond tube [26]; (d) diamond trapezoid tube [26]; (e) trapezoid origami crash box [25]; (f) origami tube with curved folds [22]; (g) origami tube with kite-shaped folds [23]; (h) half and full assembly of the arc-Miura tube [36]; (i1)-(i2) straight-crease (SC) diamond and curved-crease (CC) patterns [37]; (j1)-(j3) origami multicell tubes [27]; (k) bulkhead-reinforced origami tube [24].

adjacent faces connected by a valley fold (shown in Fig. 3 (a)) are key parameters to determine the collapse mode, peak force and plateau force, thereby influencing the EA capacity of the origami tubes.

## 2.1. Axial loading

### 2.1.1. Quasi-static loading

Research groups led by Lu and Chen [20], You [21–23], Wang [24, 25] and Xie [26,27] investigated the deformation and EA of origami tubes under quasi-static loading, and the findings are summarized here. Other similar work can be found in Refs. [28–31]. Song et al. [20] studied a square mild steel origami tube ( $M = 4$  and  $\theta = 150^\circ$ , see Fig. 3 (b)). The crushing process was investigated both experimentally and numerically, and the researchers showed that the origami-patterned tubes had a lower initial peak load and a more stable force fluctuation than those of their conventional counterparts having an identical thickness and surface area. Ma and You [21] noted that when crashing a thin-walled tube of a square section, two types of plastic hinges formed: one hinge was a stationary hinge, and the other hinges were traveling hinges that swept through an area. The latter absorbed twice as much energy as the former. Based on this, the researchers proposed a series of square origami crash boxes ( $M = 3\text{--}7$  and  $\theta = 156^\circ\text{--}172^\circ$ ) with prefolded corners involving a diamond pattern, as shown in Fig. 3 (a). The performance of one such boxes and its conventional counterpart are shown in Fig. 4. It was also found that the full diamond origami tubes had a smaller peak force because of the initial creases. In addition, it had

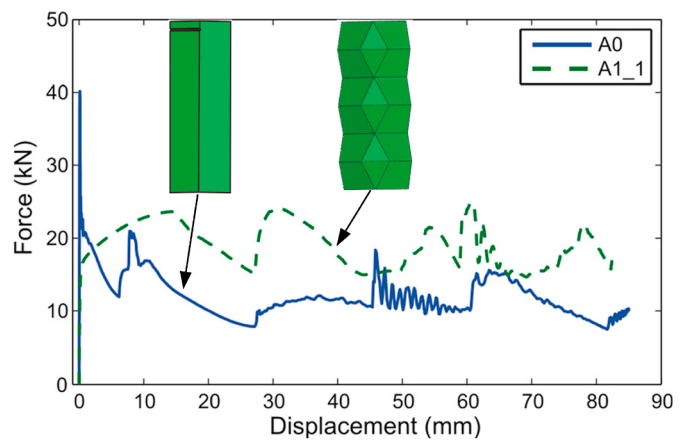


**Fig. 4.** Force-displacement curves of the conventional tube (denoted by A0) and the origami tube (denoted by as A1\_1) under quasi-static compression [21].

higher  $F_m$  and more stable force fluctuation than those of the diamond trapezoid tubes due to the changing of the deformation mode with longer plastic hinges and additional traveling hinges compared with the traditional tube. The same origami pattern was applied only on the two ends of the tube in Ref. [32] and a 46% reduction of  $F_{max}$  and a 99% increase of  $F_m$  were found. Based on the research conducted by Ma and

**Table 1**Summary of the  $F_{\max}$  reduction and  $F_m$  increase for the origami tubes.

Fig. No.	$\theta$ (°)	M	$F_{\max}$ reduction	$F_m$ increase
Fig. 3(a)	156–172	3–7	20.9% ( $\theta = 156$ , M = 6) ~ 41.0% ( $\theta = 160$ , M = 6)	56.3% ( $\theta = 160$ , M = 3) ~ 92.1% ( $\theta = 156$ , M = 6)
Fig. 3(b)	S:120–179	S: 4	S: 35% ( $\theta = 170$ ) ~ 76% ( $\theta = 120$ )	S: ~35% ( $\theta = 120$ ) ~ 3% ( $\theta = 170$ )
	H: 160–174	H:6	H: 25% ( $\theta = 174$ ) ~ 46% ( $\theta = 160$ )	H: ~12% ( $\theta = 160$ ) ~ 1% ( $\theta = 174$ )
	O:160–177	O:8	O:3% ( $\theta = 174$ ) ~ 35% ( $\theta = 160$ )	O: ~2% ( $\theta = 160$ ) ~ 28% ( $\theta = 174$ )
Fig. 3(c)	78.52	4	~0.6%–33%	2%–20%
Fig. 3(d)	84.29	4	13%–30%	~1.3%–0.6%
Fig. 3(e)	S: 156–176	S: 2	S: ~7.5% ( $\theta = 176$ , M = 2) ~ 38.6% ( $\theta = 156$ , M = 2)	S: 41.7% ( $\theta = 156$ , M = 2) ~ 53.6% ( $\theta = 176$ , M = 2)
	O: 156–176	O:3–6	O: 10.2% ( $\theta = 176$ , M = 3) ~ 44.0% ( $\theta = 156$ , M = 4)	O: 26.6% ( $\theta = 164$ , M = 5) ~ 68.0% ( $\theta = 156$ , M = 5)
Fig. 3(f)	90–175	2–7	26.2% ( $\theta = 150$ , M = 2) ~ 67.0% ( $\theta = 138$ , M = 3)	8.1% ( $\theta = 175$ , M = 5) ~ 64.9% ( $\theta = 155$ , M = 7)
Fig. 3(g)	120–168	2–6	42.3% ( $\theta = 168$ , M = 4) ~ 88.0% ( $\theta = 120$ , M = 2)	27.4% ( $\theta = 156$ , M = 6) ~ 81.6% ( $\theta = 120$ , M = 2)
Fig. 3(j1-j3)	j1: 70–80	j1: 8	j1: 14.8% ( $\theta = 80$ ) ~ 54.8% ( $\theta = 70$ )	j1: ~32.4% ( $\theta = 70$ ) ~ 7% ( $\theta = 80$ )
	j2: 70–80	j2:1	j2: 6% ( $\theta = 80$ ) ~ 46.4% ( $\theta = 70$ )	j2: ~13% ( $\theta = 75$ ) ~ 1% ( $\theta = 70$ )
	j3: 70–80	j3:8	j3: 8.3% ( $\theta = 80$ ) ~ 24.3% ( $\theta = 70$ )	j3: 3.4% ( $\theta = 70$ ) ~ 24.9% ( $\theta = 80$ )
Fig. 3(k)	156	2	~24.3% ( $t_1 = 1$ mm) ~ 1.5% ( $t_1 = 0.2$ mm)	1% ( $t_1 = 0.2$ mm) ~ 5.7% ( $t_1 = 1$ mm)

Symbol annotations: S-origami tube with square cross-section; H-origami tube with hexagonal cross-section; O-origami tube with octagonal cross-section;  $t_1$ -thickness of the bulkhead.

You [21], Yang et al. [26] investigated 3D printed octagonal brass origami tubes. Both the full diamond pattern ( $M = 4$  and  $\theta = 78.52^\circ$ , see Fig. 3 (c)) and diamond trapezoid pattern ( $M = 4$  and  $\theta = 84.29^\circ$ , see Fig. 3 (d)) were investigated, and the results from the finite element analysis (FEA) showed that the dihedral angle not only changed the  $F_{\max}$  but also affected the plateau force. The diamond trapezoid patterned tube with the dihedral angle in the range of  $145^\circ$ – $162.5^\circ$  was found to have the optimal EA capacity [33].

The diamond deformation mode is a non-symmetrical mode, which is common for thin-walled tubes under axial loading. Complete diamond mode is a desirable deformation mode for origami tubes with a low  $F_{\max}$  and high  $F_m$ . Zhou et al. [34] found that the complete diamond deformation mode increased the travel of the plastic hinges, resulting in a peak force reduction of more than 30% and an increase of more than 50% in the  $F_m$  compared with those of the conventional square tubes. However, this origami crash box design was imperfection sensitive because a symmetric deformation mode could be triggered by such unintentional imperfection, resulting in a lower  $F_m$ . This problem could be solved by modifying the dihedral angle [24]. Inspired by the previous work [20,21], Zhou et al. [25] conducted numerical quasi-static compression tests on the trapezoid origami crash boxes ( $M = 2$ – $6$  and  $\theta = 156^\circ$ – $180^\circ$ , see Fig. 3 (e)). It was shown that a lower number of modules ( $M$ ) and larger dihedral angle ( $\theta$ ) were favorable for producing the complete diamond mode, while high  $M$  and low  $\theta$  values were helpful in increasing the plateau force. The complete diamond mode was also observed during the crushing of a series of curved crease tubes (see Fig. 3 (f)), and a lower peak force was achieved [22]. However, a reduction in the average force occurred; therefore, the curved crease crash boxes did not exhibit any notable advantages over the straight crease crash box designs.

The pre-designed kirigami pattern of a tube could trigger an extensional mode under axial compression and could be regarded as geometric imperfection that effectively reduced the initial peak force [35]. Ma et al. [23] developed a kite-shaped pattern ( $M = 2$ – $6$  and  $\theta = 120^\circ$ – $168^\circ$ ) that was manufactured by bonding two pieces of origami structures folded in the Miura-ori pattern, as shown in Fig. 3 (g). The quasi-static axial crushing behaviors of this pattern were studied numerically; an  $F_{\max}$  reduction of 56.5% and an SEA increase of 29.2% was achieved compared with the characteristics of the conventional square tubes.

PVC sheets folded in the arc Miura-ori pattern were manufactured (see Fig. 3 (h)) and later spliced and bonded together, forming an arc-Miura tube [36]. A quasi-static compression test was performed, and it was observed that a large compression occurred in the middle of the tube during the experimental process. Lee et al. [37] employed pre-embedded

straight-crease (SC) diamond patterns (see Fig. 3 (i1)) and curved-crease (CC) patterns (see Fig. 3 (i2)) to control the post-buckling shape. Yang et al. [27] proposed multicell tubular structures with prefolded origami patterns, i.e., an origami quadruple-celled tube ( $M = 8$  and  $\theta = 65^\circ$ – $85^\circ$ , see Fig. 3 (j1)), origami-triggered quadruple-celled tube ( $M = 1$  and  $\theta = 65^\circ$ – $85^\circ$ , see Fig. 3 (j2)) and origami quintuple-celled tube ( $M = 8$  and  $\theta = 70^\circ$ – $80^\circ$ , see Fig. 3 (j3)). It was found that the origami tubes with quintuple cells could absorb the highest energy with a significant reduction in the  $F_{\max}$  and the crushing force fluctuation. A larger dihedral angle ( $\theta$ ) led to a higher SEA and increased the load fluctuation. However, reducing the diagonal length of the central diamond cell could reduce the load fluctuation.

A summary of the  $F_{\max}$  reduction and  $F_m$  increase for the origami tubes shown in Fig. 3 compared with the corresponding traditional tubes without origami patterns (except Fig. 3(k)) is listed in Table 1, in which the ranges of  $\theta$  and  $M$  are given. The  $F_{\max}$  reduction and  $F_m$  increase for the bulkhead-reinforced origami tube shown in Fig. 3(k) are compared with the one without a bulkhead.

### 2.1.2. Dynamic loading

In low-velocity impact, the duration of the contact between the impactor and the target is long enough for the entire structure to respond, therefore the dynamic structural response of the target is important. In contrast, in high-velocity impact, the target does not have time to respond and it is dominated by stress wave propagation through the material, which leads to localized deformation [38]. To investigate the energy absorbing performance of the materials and structures, low-velocity impact experiments are conducted, and they are usually implemented using a drop hammer with different strikers. The specimen is fixed to the ground below the drop hammer. During the test, the hammer is released, and it accelerates due to the gravity to fall on the specimen. Drop hammer tests were performed on diamond origami crash boxes (see Fig. 5 (a),  $M = 2$  or  $3$  and  $\theta = 156^\circ$ ) and reported in Ref. [34]. The complete diamond mode (see Fig. 5 (b)), the impact velocity: 7 m/s; the mass of the impactor: 64 kg, local buckling mode (see Fig. 5 (c), the impact velocity: 6 m/s; the mass of the impactor: 64 kg), and symmetric deformation mode (see Fig. 5 (d), the impact velocity: 5.5 m/s; the mass of the impactor: 64 kg) were observed during the crushing process. The force-displacement curves (see Fig. 5 (e) and (f)), indicated that the complete diamond mode is the most efficient and the symmetric mode is the least efficient among the three modes in terms of the EA [34].

In addition to the quasi-static behavior, Ma and You [21] investigated the dynamic behavior of origami crash box ( $M = 3$  and  $\theta = 160^\circ$ , see Fig. 3 (b)) by using the ABAQUS/Explicit program, with an impact

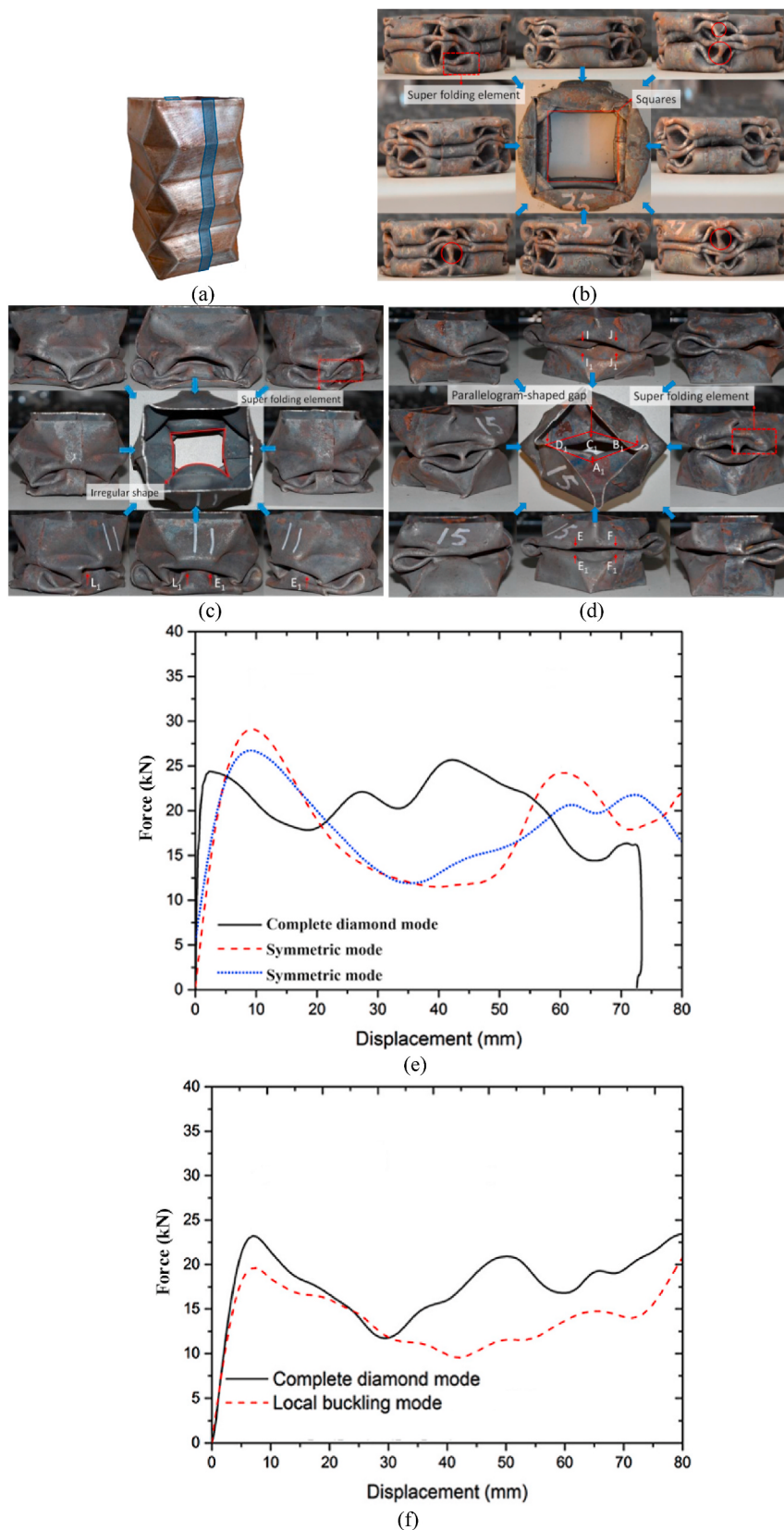


**Fig. 5.** Collapse modes and force-displacement curves under a drop hammer impact. (a) Undeformed origami tube; (b) complete diamond mode; (c) local buckling mode; (d) symmetric mode; (e) comparison of the force-displacement curves of the complete diamond mode and symmetric mode; (f) comparison of the force-displacement curves of the complete diamond mode and local buckling mode [34].

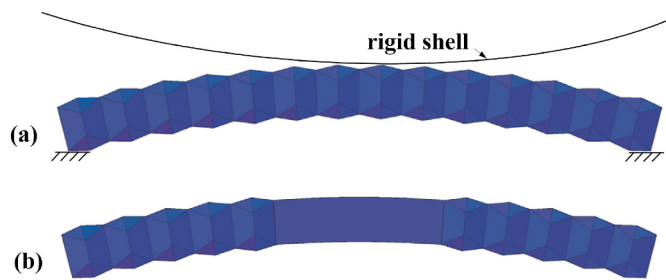


**Fig. 6.** Origami tubes for lateral impact. (a) The full origami tube; (b) the partial origami tube [45].

speed of less than 20 m/s. The origami crash box was appropriate to be used for the impact loadings because the complete diamond mode was still generated under the dynamic loading. The origami crash boxes ( $M = 5$  and  $\theta = 156^\circ$ ) subjected to an oblique loading at  $0^\circ$ – $30^\circ$  to the axial direction of the tubes were also investigated [39]. It was found that in terms of the SEA, the origami crash boxes performed better than a conventional square tube in most of the load angle range. Inspired by

bamboo nodes and nodal diaphragms, a bulkhead-reinforced origami crash box (see Fig. 3 (k)) with optimized folded lobe width and bulkhead thickness exhibited a high performance under oblique loading [39]. The bulkhead could significantly alter the deformation mode of the tube from the symmetric mode to the complete diamond mode or the transition mode [24]. However, the dynamic effects on the deformation mode and EA capacity due to high strain rates, inertia and stress waves were not observed, because the impact velocity from the drop hammer was not sufficiently large to change the mode of deformation. Therefore, further work should be conducted considering the high-velocity impact on the origami tubes.

## 2.2. Lateral loading

Automobile bumpers and roadside guardrail systems are normally made from thin-walled beams to absorb the kinetic energy of a vehicle during a collision. Shallow curved profiles with an open or closed cross-section are often adopted to reduce not only the injuries to the passengers but also the damage to the vehicles [40,41]. Conventional thin-walled beams with different cross-sections under lateral loading

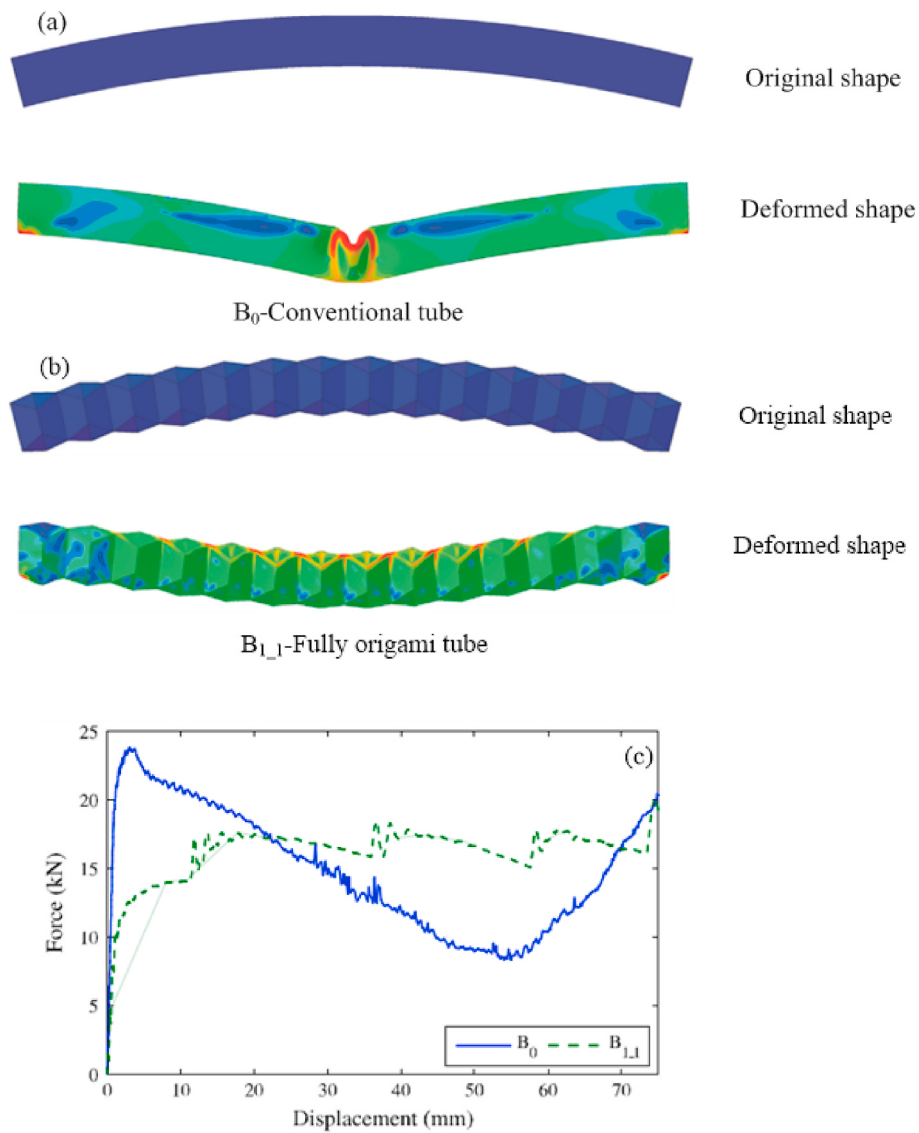


**Fig. 7.** Comparison of the conventional tube ( $B_0$ ) and a full origami tube ( $B_{1\_1}$ ) with the same radius of curvature and length under a lateral bending loading. (a) Deformation of the conventional tube, as determined using the FEA; (b) deformation of the origami tube, as determined using the FEA; (c) force-displacement curves [45].

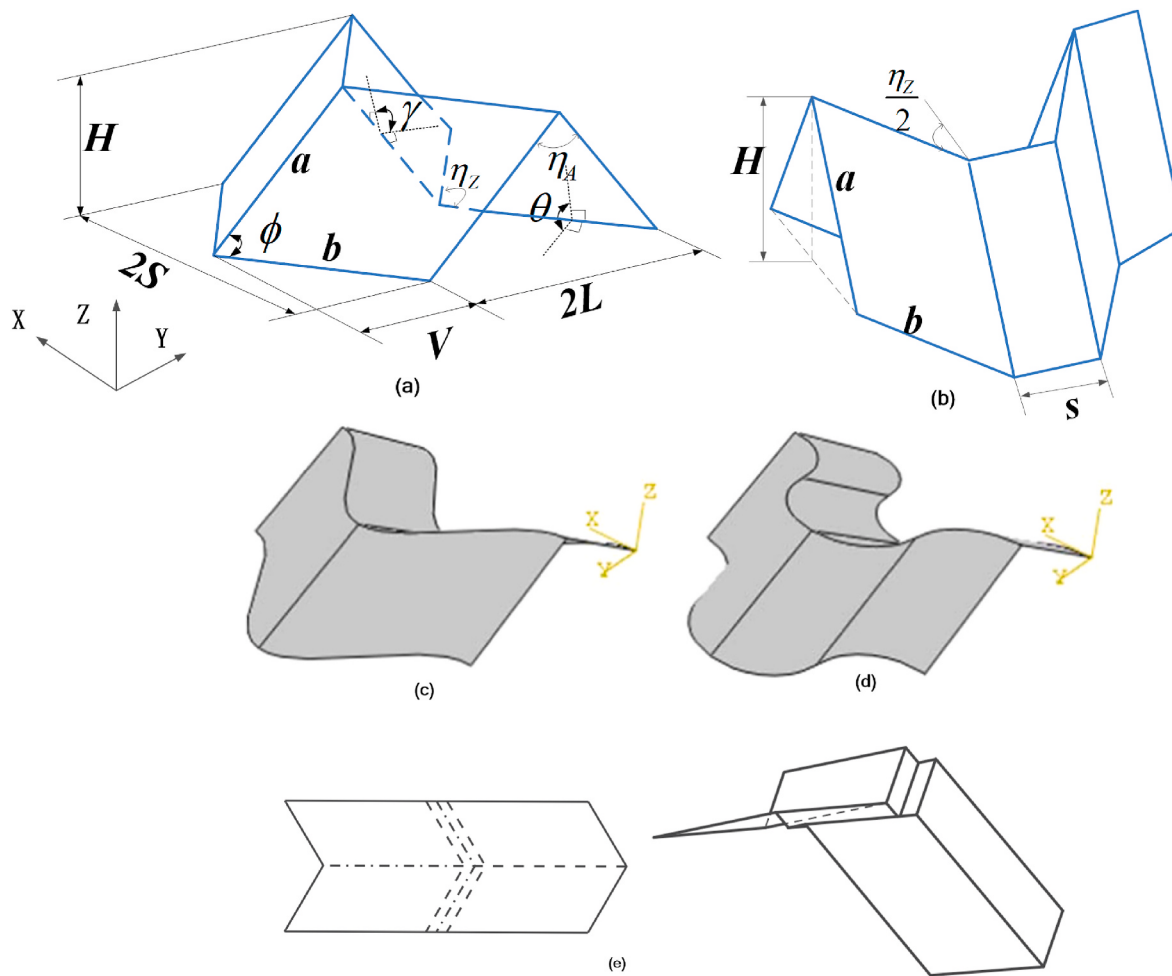


**Fig. 8.** Various foldcore units. (a) Miura foldcore [61] (b) trapezoidal wave pattern [61]; (c) sinusoidal wave pattern [61]; (d) piecewise elliptical wave pattern [61]; (e) indented Miura pattern [52].

have been investigated both experimentally and analytically [42,43]. Recent work has demonstrated that origami thin-walled tubes can also be used as energy absorbers in such applications.

The research group of You [44,45] studied both experimentally and numerically a series of thin-walled tubes with origami patterns subjected to lateral crushing. Ma and You [45] proposed two curved thin-walled tubes: the full and partial origami tubes, as shown in Fig. 6 (a) and (b). A rigid shell with an identical radius of curvature of the beam moved downward to compress the beam, shown in Fig. 6 (a). The lower edge of each end of the beam was clamped as shown in Fig. 6 (a). Three collapse modes, namely, the bending collapse (global bending of the whole tube), longitudinal folding (local deformation of the origami patterns), and mixed mode (bending collapse and longitudinal folding simultaneously) were observed. The loading and boundary conditions for the beams in Fig. 7 (a) and (b) are the same with those in Fig. 6. For a conventional thin-walled tube of the same profile, local buckling occurred first in the midspan, followed by the formation of a localized plastic hinge, as shown in Fig. 7 (a). However, for the full origami tube, no localized plastic hinge occurred, and the plastic deformation was dispersed along the entire tube as shown in Fig. 7 (b). Consequently, a remarkably smooth force-displacement curve was obtained, as indicated by the dashed green line in Fig. 7 (c), which demonstrated that the energy dissipation rate was stable. The origami tube achieved a peak force reduction of 15.4% and an increase of 6.3% in the SEA, compared with those of the conventional counterpart having the same profile. The mixed mode for the partial origami tube was found to be the most efficient under a quasi-static loading in terms of the EA. A dynamic

analysis also showed a similar trend.

### 3. Origami plate structures

#### 3.1. Origami foldcores

The foldcore is a structure created by folding a sheet material using a tessellation origami pattern, some of which are shown in Fig. 8. The most popular pattern used for this purpose is the Miura-ori pattern, which we shall refer to as the Miura foldcore hereafter for brevity.

Each face of a Miura-ori pattern is considered as a rigid body, and the motions can be modeled kinematically by treating the creases as perfect line hinges. A unit consists of four identical parallelograms, as shown in Fig. 8 (a). When the side lengths  $a$  and  $b$  and sector angle  $\varphi$  are given, the motion state of the unit is dependent on the dihedral angle  $\theta$ . The dimensions  $V$ ,  $L$ ,  $S$ , height  $H$  and dihedral angle  $\gamma$  can be expressed in terms of the dihedral angle  $\theta$  as follows:

$$S = b \sin \varphi \sin\left(\frac{\gamma}{2}\right) = \frac{b \sin \alpha \cos \theta}{\sqrt{1 - \sin^2 \varphi \sin^2 \theta}} \quad (1)$$

$$L = \sqrt{a^2 - H^2} = a \sqrt{1 - \sin^2 \varphi \sin^2 \theta} \quad (2)$$

$$V = b^2 - S^2 = \frac{2ab \cos \varphi}{L} \quad (3)$$

$$H = a \sin \varphi \sin \theta \quad (4)$$

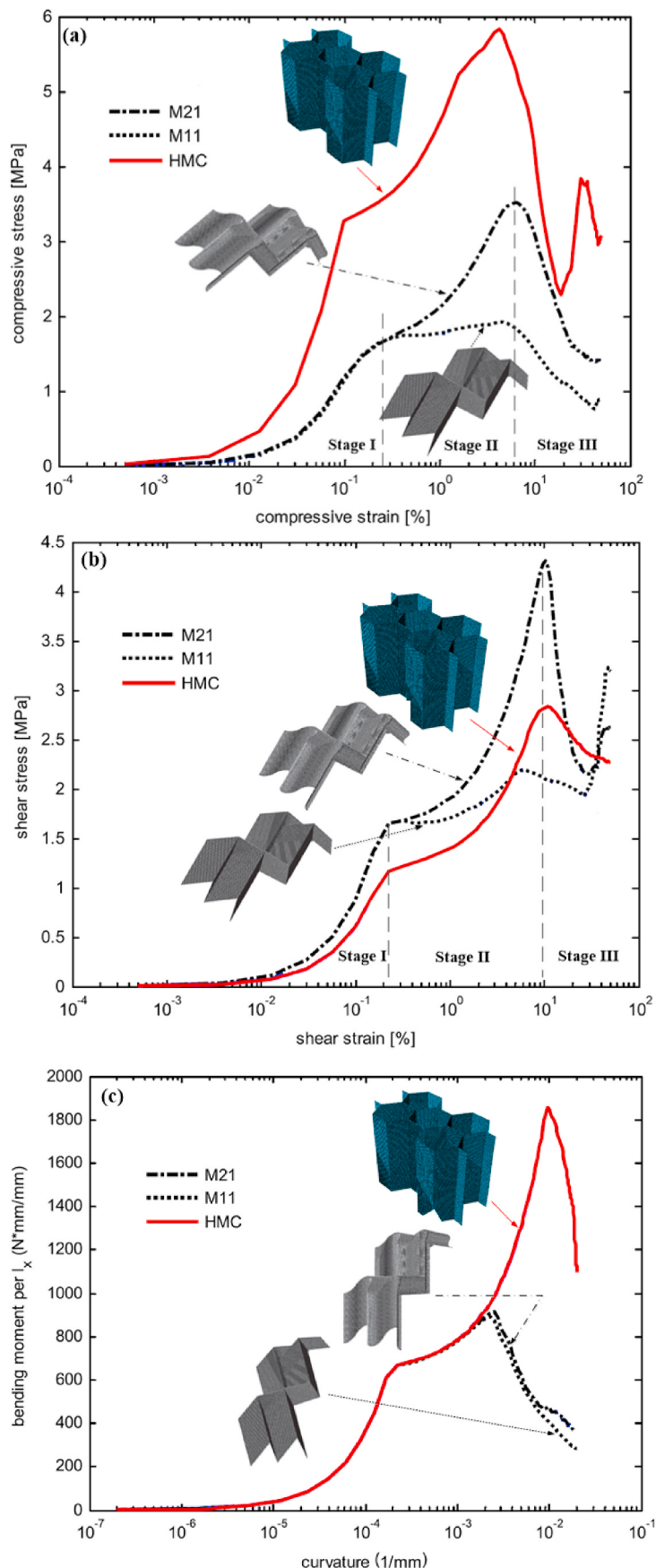


**Fig. 9.** Results from the numerical study. (a) Stress-strain curves for the compression test; (b) stress-strain curves for the shear test (Y-Z plane; the X, Y, Z directions are shown in Fig. 8 (a)); (c) normalized bending moment-curvature curves for the bending test (X direction) [48] (---- M21 denotes the Miura core with curved creases consisting of four unit cells in a  $2 \times 2$  array; ..... M11 denotes the typical Miura core consisting of four unit cells in a  $2 \times 2$  array; —— HMC denotes the honeycomb core.).

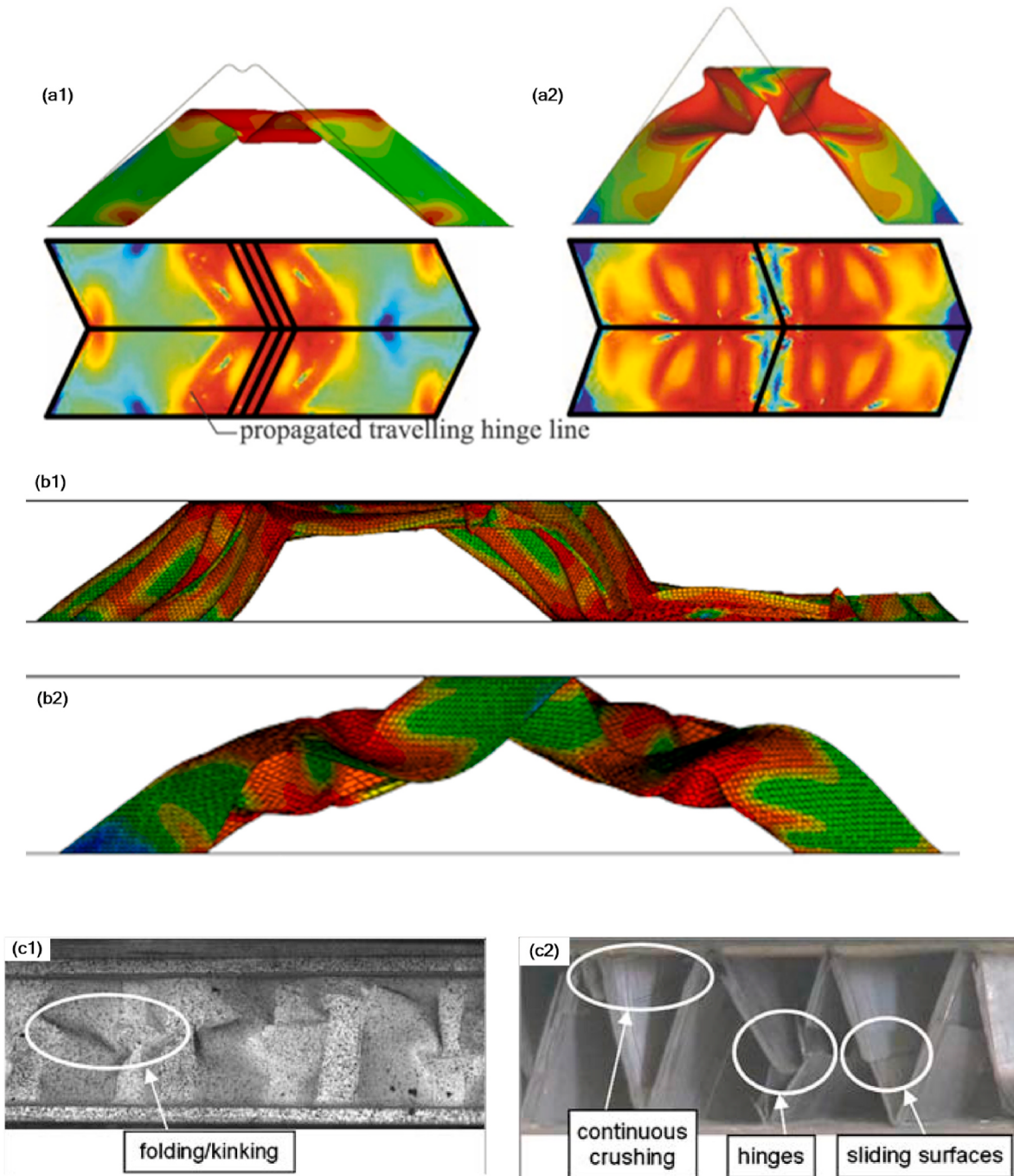


**Fig. 10.** Failure and deformation modes. Deformation mode of (a1) the indented foldcore cell and (a2) the conventional Miura foldcore [52]; deformation mode of (b1) the multicorrugated indented foldcore cell and (b2) the Miura foldcore [14]; (c1) kinking of the cell wall and (c2) crushing of the cell wall [55].

$$\gamma = 2 \arcsin \frac{\cos \theta}{\sqrt{1 - \sin^2 \theta \sin^2 \varphi}} \quad (5)$$

The typical geometrical parameters of the unit cells of the Miura foldcore and other commonly used foldcores are given in Fig. 8. The in-plane compression is defined as the compression in the X or Y direction (see Fig. 8 (a)), while the out-of-plane compression is defined as the compression in the Z direction (see Fig. 8 (a)).

To describe the mechanical characteristics related to the strength and EA capacity of a Miura origami unit cell under the in-plane compression (X direction), Zhang et al. [46] proposed an analytical model of the quasi-static response and the expressions of the quasi-static compression force  $F_c$  and SEA are shown below.

$$F_c = \sigma_m t^2 \frac{(1 + \cos^2 \theta \tan^2 \varphi)^{1/2}}{\tan \varphi} \left[ \frac{(1 + \cos^2 \theta \tan^2 \varphi)}{\sin \theta} + \frac{a}{b} \frac{1}{\sqrt{\cos^2 \varphi (1 + \cos^2 \theta \tan^2 \varphi) - \cos^2 \theta}} \right] \quad (6a)$$

$$W = 2b \tan \varphi \left[ \frac{\cos \theta}{(1 + \cos^2 \theta \tan^2 \varphi)^{1/2}} - \frac{\cos \theta_0}{(1 + \cos^2 \theta_0 \tan^2 \varphi)^{1/2}} \right] \quad (6b)$$

$$SEA = \frac{\sigma_m}{\rho_m} \frac{1}{\rho_0^* \cdot A(\theta_0) \cdot 2S(\theta_0)} \int_0^{|W_f|} \frac{F_c(\xi)}{\sigma_m} d\xi \quad (7)$$

where  $\theta \in [\theta_0, 90^\circ]$ ;  $\theta_0(\gamma_0)$  is the initially folded pattern;  $t$  is the thickness of the cell wall;  $\sigma_m$  and  $\rho_m$  are the yield stress and the density of the base material, respectively;  $W$  is the external work;  $\rho_0^*$  is the relative density of the Miura-ori sheet;  $A$  is the area in the Y-Z plane;  $F_c(\xi)$  is defined by Eq. (6a). Using  $\theta$  as a process parameter in Eq. 6 (a-b), the force-displacement history  $F_c(W(\theta))$  was obtained.

Lv et al. [47] carried out analyses on the response of Miura-ori sheets under compression loading in the out-of-plane direction. From the observation of the FEA results, when the cell wall started to buckle,  $F_{\max}$  occurred. Based on Euler's theory of elastic buckling, one piece of the cell wall was treated as a regular column and gave empirical formulae for the dimensionless parameter  $F_{\max} \cos \theta / Et^2$ , as follows.

$$\text{When } t/a < 0.033 \text{ (i.e., } a/t > 30\text{), } \frac{F_{\max} \cos \theta}{Et^2} = 3.16 \left( \frac{t}{a} \right)^{0.34} \quad (8)$$

$$\text{when } t/a > 0.033 \text{ (i.e., } a/t < 30\text{), } \frac{F_{\max} \cos \theta}{Et^2} = 0.98 \quad (9)$$

After the peak force, the force decreased with the compression displacement. To analyze the EA performance during this stage, the  $F_m$  of a load-displacement curve was used. An empirical formula of the dimensionless parameter  $F_m (\cos \theta)^{0.44} / \sigma_y t^2$  was given,

$$\frac{F_m (\cos \theta)^{0.44}}{\sigma_y t^2} = 87.98 \quad (10)$$

### 3.1.1. Metallic foldcores

Zhou et al. [48] stated that both the out-of-plane compression and in-plane shear behaviors of the Miura foldcore and a honeycomb core having the same density ( $\rho = 0.05\rho_m$ , where  $\rho_m$  is the density of the base material, aluminum alloy) could be characterized by three distinct stages: I: prebuckling, II: folding, and III: densification (see Fig. 9 (a) and (b)). In Ref. [48], model M11 ( $a = 10\sqrt{2}$  mm,  $H = 10$  mm,  $S = 5$  mm and  $L = 10$  mm) had the best EA performances under compressive and shear loads; therefore, modified foldcores with curved fold lines based on model M11, for example, M21 with a radius of curvature  $\pi/4$  (see Fig. 9

(a) and (b)), were proposed. The results indicated that the Miura-based folded cores had a comparable or better stiffness and strength under the shear and bending loadings in comparison with those of the honeycomb core (see Fig. 9 (b) and (c)); however, the Miura-based folded cores displayed a considerably lower stiffness and strength under compression (see Fig. 9 (a)) [48–50]. Fischer [51] compared an aluminum Miura foldcore ( $H = 12$  mm,  $L = 6.28$  mm,  $S = V = 8.84$  mm,  $\rho = 0.02\rho_m$ , see Fig. 8 (a)), an aluminum honeycomb of a similar density and an aluminum foam with a higher density ( $\rho = 0.09\rho_m$ ), and found that the in-plane shear stiffness and strength of the Miura foldcore were slightly lower than those of the honeycomb, whereas the foam presented the lowest stiffness and strength among the three structures. The quasi-static out-of-plane compression behavior of the Miura-ori patterned sheets (a

$= b = 20$  mm,  $\varphi = 60^\circ$ ,  $\theta = 50^\circ$ ,  $H = 13.27$  mm,  $S = 14.88$  mm,  $L = 14.97$  mm, and  $\gamma = 118.42^\circ$ , refer to Fig. 8 (a)) was investigated experimentally [47]. A parametric study was also conducted numerically, and the results showed that a larger  $t$  or smaller  $\varphi$  led to a higher stiffness and load carrying capacity. The structure with a smaller  $\varphi$  had a lower peak force and a higher  $F_m$ , which is favorable in the design of protective structures.

To increase the overall EA, indentations was added to a typical Miura foldcore (see Fig. 8 (e)) by Gattas and You [52], who aimed to activate the traveling plastic hinges, as in the origami crash boxes reported in Ref. [19]. The researchers found that the out-of-plane quasi-static compressive load provoked a new failure mode known as the high order traveling hinge line (see Fig. 10 (a1)) with a considerably higher and more uniform EA compared with the conventional Miura foldcore (see Fig. 10 (a2)). Fig. 10 (b1) shows that the dents worked as the hinges during the crushing process, and a higher EA was achieved. Furthermore, Gattas and You [52] numerically and experimentally examined the Miura foldcore with curved creases (see Fig. 8 (c) and (d)) and found that the curved crease foldcores had a significantly higher EA capabilities under a quasi-static compressive load. Li and You [45] further investigated the multi-corrugated indented foldcores obtained by merging the curved-crease and indented Miura foldcores, and found that this configuration resulted in an increase in the EA. Zhou et al. [48] conducted a parametric study using FEM on the mechanical properties of a series of modified Miura foldcores made from aluminum alloy, including the curved crease (see Fig. 8 (c)) and double layered Miura foldcores. It was noted that the foldcores with the curved folds performed better in terms of the stiffness and strength under both the compression and shear loadings, while the double layered foldcores exhibited a larger stiffness and strength in bending.

### 3.1.2. Composite foldcores

Metallic foldcores absorb energy mainly through the stationary plastic hinges and traveling hinges, while foldcores made from composite sheet materials have different failure modes. Grzeschik et al. [53] studied the mechanical properties of the Miura foldcores made from aramid paper ( $H = 12.7$  mm,  $L = 5.35$  mm,  $S = V = 5.3$  mm, refer to Fig. 8 (a)). The researchers found that the aramid paper foldcores exhibited a lower out-of-plane compressive strength but a considerably higher in-plane shear strength and stiffness in the X direction (see Fig. 8 (a)) compared with those of the aramid paper honeycomb and

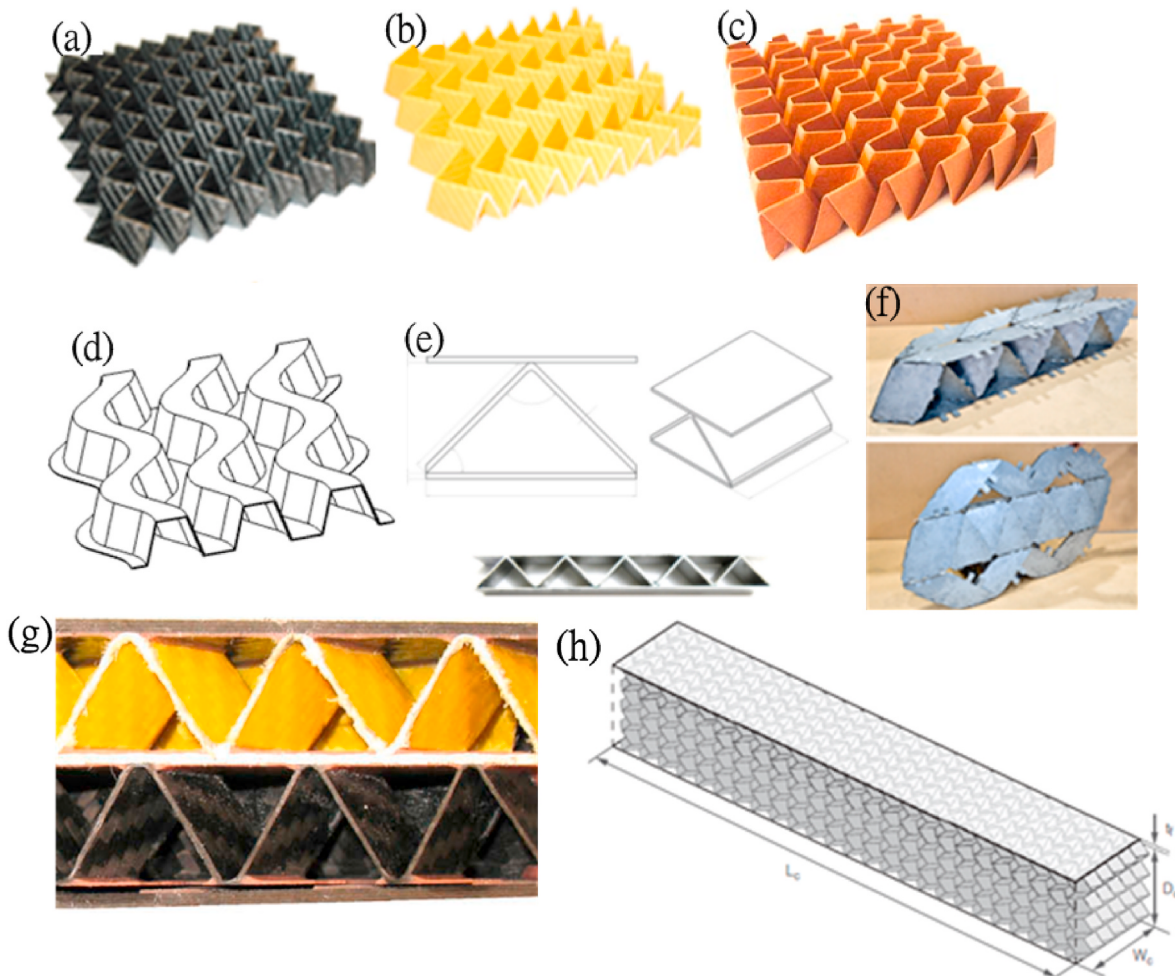


**Fig. 11.** (a) Carbon fiber Miura foldcore [64]; (b) aramid fabric Miura foldcore [64]; (c) aramid paper foldcore: trapezoidal wave pattern [55]; (d) m-shaped foldcore [71]; (e) corrugated core sandwich panels [70]; (f) morphing sandwich beam [77]; (g) a double layered core with a combination of a carbon foldcore, an aramid foldcore, and an aramid composite middle layer [64]; (h) stacked sandwich structure with a foldcore [79].

polymethacrylimide foam with the same density,  $\rho = 32 \text{ kg/m}^3$ . However, compared with a aramid paper foldcores with a trapezoidal wave pattern ( $\eta_s=61^\circ$ ,  $H = 20 \text{ mm}$ ,  $b = 12.5 \text{ mm}$ ,  $s = 5 \text{ mm}$ , refer to Fig. 8 (b)), a aramid paper honeycomb core performed better in terms of the out-of-plane compression strength, modulus, and in-plane shear strengths, while the foldcores had a higher shear modulus [54].

The out-of-plane compressive behavior of the aramid paper and carbon fiber-reinforced plastic (CFRP) folded cores was studied both experimentally and numerically [55]. The densities were approximately  $\rho = 113 \text{ kg/m}^3$  for the aramid paper Miura foldcore and  $\rho = 102 \text{ kg/m}^3$  for the CFRP Miura foldcore. Two different failure modes were found: the kinking of the cell walls for the aramid paper foldcore (see Fig. 10 (c1)) and the crushing of the cell walls for the CFRP foldcore (see Fig. 10 (c2)). Fischer et al. [56] obtained the stress-strain curves of the aramid paper Miura foldcores ( $0.03\rho_m < \rho < 0.19\rho_m$ ). Under shear loading, the foldcore exhibited elastic properties until a peak force. Jiang et al. [57] conducted the out-of-plane compression tests on carbon and Kevlar Miura foldcores ( $\varphi=60^\circ$ ,  $\eta_s = 45^\circ$ ,  $\eta_A = 45^\circ$ ,  $a = b = 12 \text{ mm}$ ,  $H = 10 \text{ mm}$ , refer to Fig. 8 (a)), and their result showed that the compression strength and modulus were considerably increased along with the core wall thickness.

### 3.1.3. Thermoplastic foldcores

The deformation behavior of a thermoplastic foldcore for out-of-plane compression [58–60] and in-plane compression [58] was investigated both experimentally and numerically. It was found that the

Miura foldcore made from a copolymer Elvaloy sheet ( $\varphi = 60^\circ$ ,  $\theta = 54^\circ$ ,  $\gamma = 110.9^\circ$ ,  $a = b = 10.5 \text{ mm}$ ,  $H = 7.3 \text{ mm}$ ,  $L = V = S = 7.5 \text{ mm}$ , refer to Fig. 8 (a)) absorbed 50% more energy in the Y direction than in X direction (the X and Y directions are shown in Fig. 8 (a)) [58]. The main deformation was found to be elastic in the in-plane compression tests, and in the three-point bending test, no plastic deformation occurred [58]. Zang et al. [61] compared four different Miura foldcores made of thermoplastic material ( $H = 15 \text{ mm}$ ,  $0.026\rho_m < \rho < 0.029\rho_m$ , see Fig. 8 (a)–(d)). After the elastic deformation stage, plastic deformation occurred when the stress value decreased rapidly due to the facet buckling, folding and crack initiation and propagation. Besides, the compressive strength and shear strength were found to be sensitive to the denseness of the foldcore in the transverse or longitudinal direction. It was found that all the three modified Miura foldcores (see Fig. 8 (b)–(d)) had a higher EA capability than that of a typical Miura foldcore (see Fig. 8 (a)), which meant that the piecewise elliptical pattern outperformed the other patterns. The result indicated that despite the lower compressive and shear stiffness and strength, the polyether ether ketone (PEEK) foldcore exhibited a comparable or even better EA performance than that of the aramid foldcore owing to the better ductility of the PEEK [61].

### 3.2. Sandwich plates with origami foldcore

Sandwich plates are formed by bonding the top and bottom skins to the origami foldcores. Heimbs [62] provided an overview of the family

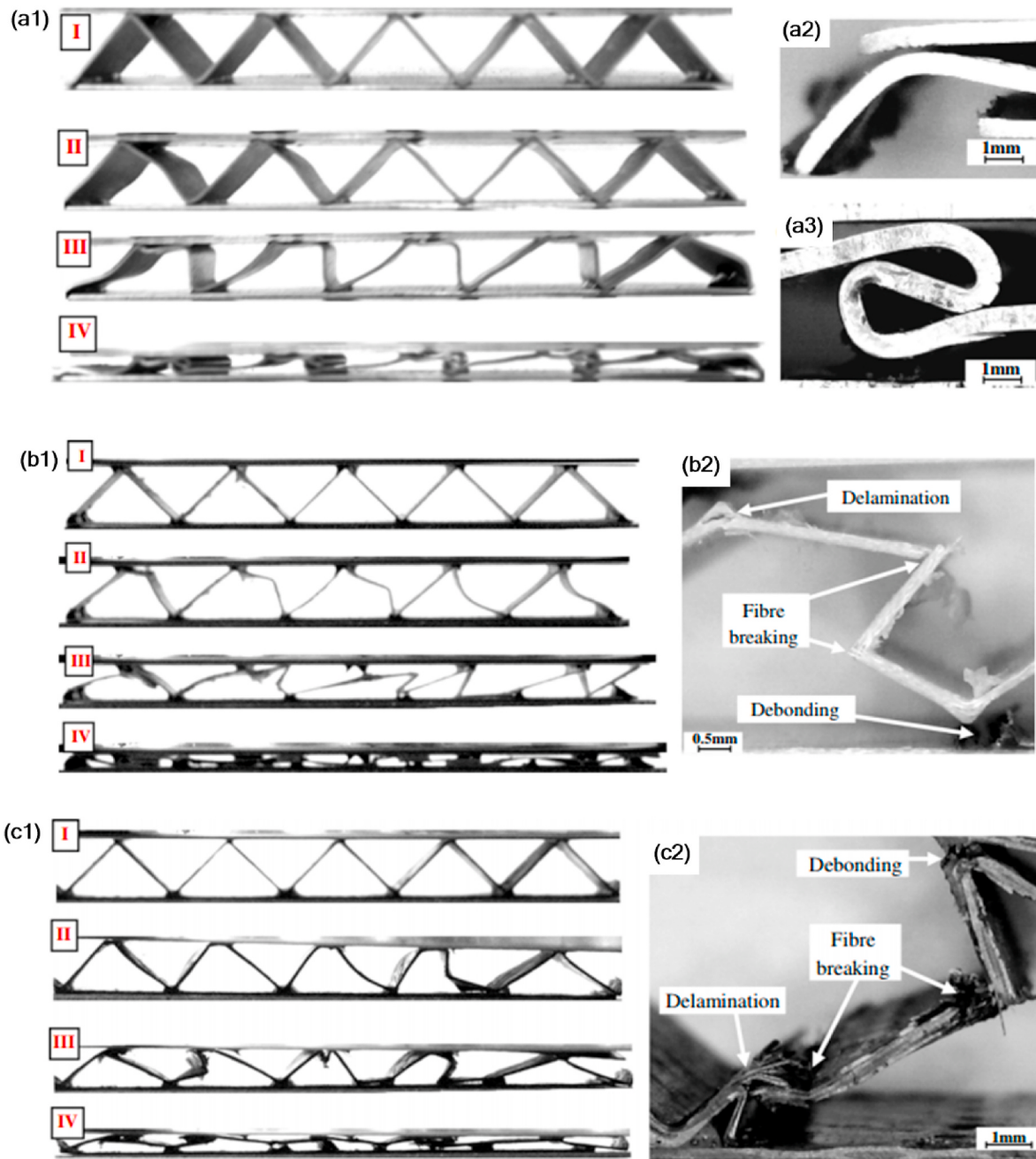


Fig. 12. Failure of sandwich structures with a foldcore: (a) aluminum alloy; (b) GFRP; and (c) CFRP under compression test [70].

of composite foldcore sandwich structures with a focus on their impact performance. The foldcore design can be adjusted easily by changing the geometrical parameters [54,63]. Different geometries were reviewed for aluminum foldcore [51], carbon fiber foldcore (see Fig. 11 (a)) [64,65], aramid paper foldcore (see Fig. 11 (b) and (c)) [55,56,64], and thermoplastic, such as PEEK and polyethylene terephthalate (PET) foldcores [61], to identify the influences of their geometrical parameters under the static compression or shear loadings. Heimbs summarized [62] the impact performances for low-velocity [64–67] and high-velocity impacts with different projectiles such as steel balls, steel cubes, steel bars, tire rubber, and hailstones [51,64,68,69].

### 3.2.1. Quasi-static loading

The stiffness, strength, displacement, fatigue and failure modes are the main concerns for materials and structures under quasi-static loading. Quasi-static compression [64,70,71], torsion [72], shear [51,

64], bending [51,73,74], combined compression-shear [75] and combined bending-compression [63,76] tests have been conducted on foldcore sandwich structures. Elastic buckling, crushing fracture of the cell walls and delamination were observed to control the strength of a composite sandwich structure with an m-shaped foldcore (see Fig. 11 (d)), and no bond failure was observed [71]. Before any visible failure, the peak stress for foldcores with  $\rho = 0.028\rho_m$  and  $0.042\rho_m$  occurred at 1.12 MPa and 2.86 MPa, respectively; this phenomenon was followed by buckling and the subsequent large bending deformation of the cell walls. For foldcores with  $\rho = 0.056\rho_m$  and  $\rho = 0.06\rho_m$ , the dominant failure mode was the crushing fracture of the cell walls. The failure mechanisms of the corrugated core sandwich panels (see Fig. 11 (e)) made of aluminum alloy, glass fiber-reinforced plastic (GFRP), and CFRP were studied [70]. The initial failure mode was the buckling of the cell walls (see Region II in Fig. 12 (a1), (b1) and (c1)). The aluminum corrugations deformed in a plastic manner, and localized plastic hinges were visible

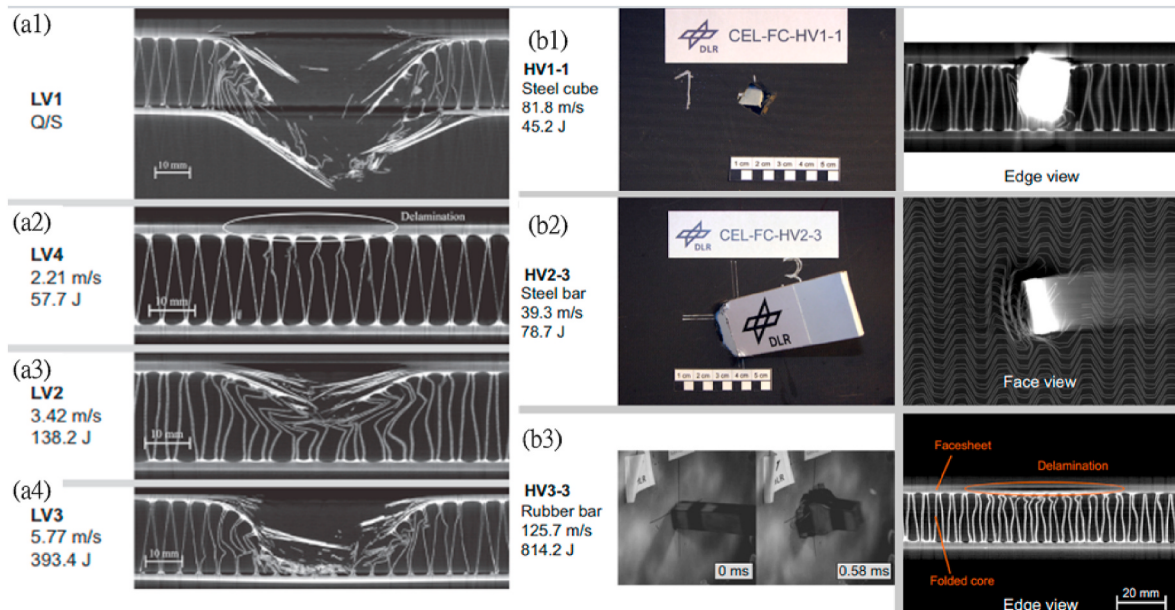


**Fig. 13.** Sandwich panel with an aramid foldcore and CFRP skins impacted by an indenter in: (a) quasi-static and low-velocity impact tests and (b) high-velocity impact tests [80].

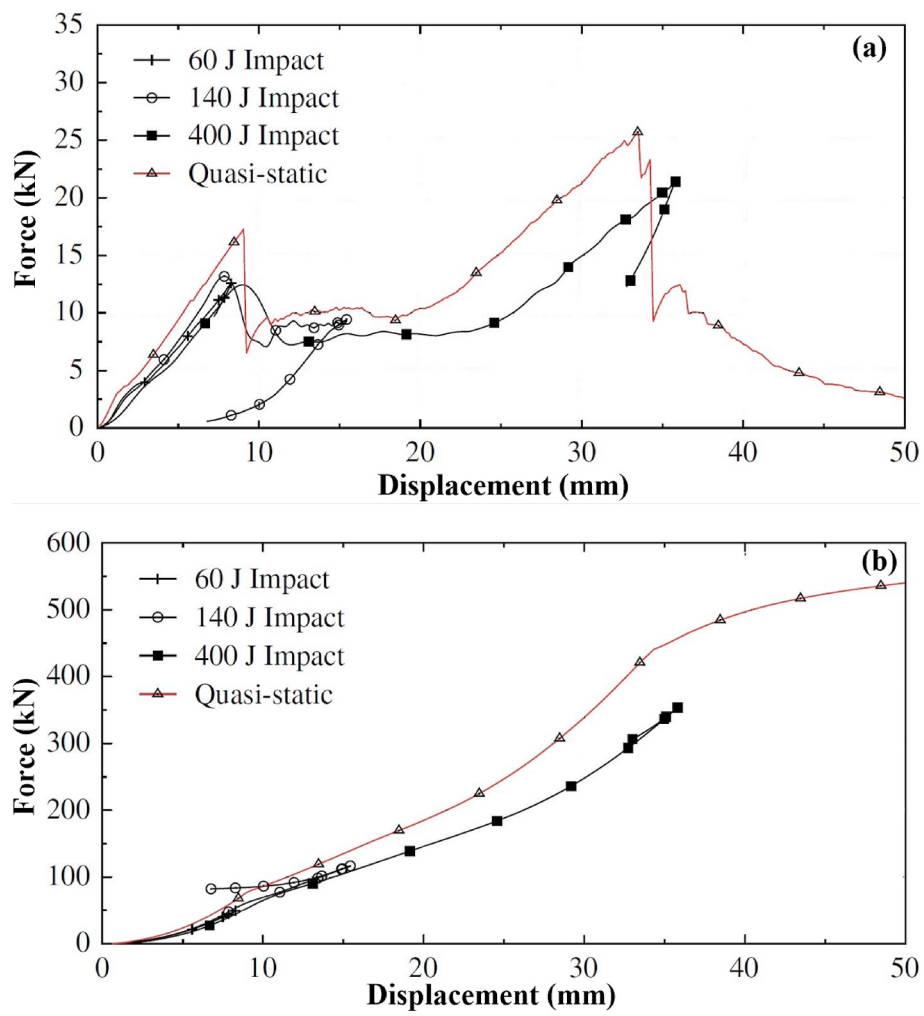


**Fig. 14.** Results from the quasi-static and dynamic impact tests. (a) Load-deflection curves and (b) absorbed energy-deflection curves [67].

(see Fig. 12 (a)). The failure modes of the GFRP and CFRP cores were similar, i.e., the buckling of the cell walls occurred first; this phenomenon was followed by the fracture of the fibers and debonding between the core and the skin, and the delamination occurred (see Fig. 12 (b) and (c)). The specific out-of-plane compressive stiffness and strength of the thick CFRP corrugations, defined as the stiffness/strength per unit mass, were similar to those of the aluminum honeycombs. All these composite sandwich structures were found to significantly outperform the structures with conventional polymer and metal foam cores in terms of the specific out-of-plane compressive stiffness and strength. Three-point bending tests were performed on the GFRP foldcore sandwich beams ( $\eta_z = \eta_A = 90^\circ$ ,  $a = 28.28$  mm,  $b = 21.21$  mm,  $H = 15$  mm, refer to Fig. 8 (a)), both experimentally and numerically [73]. Core buckling in the relatively thin-walled cores and core bending and interfacial debonding in the thick-walled cores were observed. The foldcore structures were tested under combined compression-shear (Miura foldcore:  $b = 33$  mm,  $H = 28$  mm,  $S = 17.5$  mm,  $L = 9$  mm,  $\rho = 58$  kg/m<sup>3</sup>, refer to Fig. 8 (a)) [75] and bending-compression conditions (foldcore using trapezoidal wave pattern:  $s$  was increased from 5 mm up to 15 mm in steps of 2.5 mm, refer to Fig. 8 (b)) [76]. It was found that a aramid paper honeycomb core performed better in terms of the out-of-plane compression strength, modulus, and in-plane shear strengths, while a aramid paper foldcores had a higher shear modulus [54]. However, Heimbs et al. [64] found that the out-of-plane compression stiffness and strength of the sandwich structures with the carbon foldcores ( $b = 18$  mm,  $H = 28$  mm,  $L = 7.5$  mm,  $S = 15.5$  mm,  $\rho = 0.28\rho_m$ , refer to Fig. 8 (a)) were better than those of the Nomex honeycomb cores with a similar density, which provided a representative example of how the properties of the foldcore can be adjusted through the selection and optimization of the appropriate geometry and material parameters for specific requirements.

The sandwich structures with Miura foldcores exhibit an efficient load transfer behavior. However, these configurations cannot be used for deployable structures because the bonds of the face sheets and core prohibit the foldability of the cores of these structures [77,78]. A morphing sandwich beam (Miura foldcore: ( $\varphi = 65.9^\circ$ ,  $\gamma = 90^\circ$ ,  $\eta_z = 80.2^\circ$ ,  $\eta_A = 64.2^\circ$ ,  $a = 283$  mm,  $b = 232$  mm,  $H = 25$  mm, refer to Fig. 8 (a)) was proposed by Gattas's research group (see Fig. 11 (f)) [77] by using discontinuous skins. Due to the eccentricity and flexibility of the face sheets, under a three-point bending test, the peak force and EA were reduced by 44% and 47%, respectively, in comparison with those of a foldcore sandwich beam with the same geometrical parameters.

### 3.2.2. Dynamic loading

#### (a) Low-velocity loading

Different failure modes appear under low-velocity loading for sandwich panels, including skin damage or skin penetration, core micro-buckling and core penetration, depending on the indenter type and impact energy [80]. Low-velocity impact tests are usually performed first and three-point [81] or four-point [54,82] bending tests are later conducted to determine the residual properties of the post-impact sandwich structures.

Sandwich panels with an aluminum Miura foldcore ( $H = 12$  mm,  $L = 6.28$  mm,  $S = V = 8.84$  mm,  $\rho = 0.02\rho_m$ , refer to Fig. 8 (a)) were impacted by a steel ball, both experimentally and numerically [51]. From the FEA, it was found that a core failure and plastic deformation of the outer face sheet occurred for even a low impact energy of less than 5 J; for a higher energy impact, the densification of the core, large plastic deformation of the face sheets and bending of the entire specimen occurred. The sandwich structures with aramid/phenolic Miura foldcore and CFRP skins subjected to spherical impact at several velocities were also tested experimentally and numerically [67,80]. The FEA performed in Ref. [67] indicated that a core failure and plastic deformation of the outer face sheet occurred for even a low impact energy of less than 5 J. In contrast, for a higher energy impact, as shown in Fig. 14 (a) and (b), a

larger force and EA occurred in the quasi-static test than in the dynamic tests. Under a low impact velocity, the impact ball caused a delamination on the outer skin at the contact position (see Fig. 13 (a2)). Under a relatively high impact velocity, the core absorbed the remaining impact energy and protected the inner skin from damage after the outer skin penetration (see Fig. 13 (a3)). When the impact velocity reached 5.77 m/s (393.4 J), the core was crushed completely after the outer skin penetration; however, the inner skin was not fractured (see Fig. 13 (a4)). The carbon fiber and aramid paper Miura foldcore sandwich panels ( $H = 28$  mm,  $L = 7.5$  mm,  $S = 15.5$  mm,  $\rho = 0.28\rho_m$ , refer to Fig. 8 (a)) were tested with impact energies ranging from 5 J to 60 J [64]. A local crushing of the carbon foldcore occurred under even extremely low impact energy, while the aramid foldcore behaved in a more ductile manner. The interlaminar failure started when the impact energy reached 20 J. It was found that the neighboring zigzag-patterned cell walls acted as the delamination stoppers. A double layered Miura foldcore, including a carbon Miura foldcore and an aramid Miura foldcore as well as an aramid composite middle layer (see Fig. 11 (g)) subjected to low and high-velocity impacts was also investigated [64]. When the impact energy reached 60 J, the impactor was still blocked by the upper layer. Therefore, the multicore configuration showed a satisfactory impact performance in terms of the impact energy and residual strength.

#### (b) High-velocity impact

Gas guns are used in high-velocity impact tests in which a projectile is accelerated by the gas pressure inside a barrel. Three outcomes may occur at the end of the impact test: (1) The projectile bounces back from the outer skin; (2) the projectile gets stuck in the target structure; or (3) the projectile penetrates the entire target structure [62]. Two important physical quantities are used to assess the perforation resistant behavior and EA performance of the target structure, namely, the ballistic limit and perforation energy. The ballistic limit is defined as the velocity at which the projectile is either stuck in the target structure or penetrates it with a negligible velocity. The perforation energy is the energy loss of the projectile during the perforation [83]. The ballistic limit and energy absorbing performance are the main concerns for materials and structures under a high-velocity impact.

Aluminum [51], carbon fiber [64], and aramid paper [64,80] foldcore sandwich panels were tested under high-velocity impacts, both experimentally and numerically. A steel cube (mass: 13.4 g) and a steel bar (mass: 100 g) were used to impact the sandwich panels with a carbon fiber Miura foldcore and double layered Miura foldcore ( $H = 14$  mm,  $L = 7.5$  mm,  $S = 15.5$  mm, refer to Fig. 8 (a)) [64]. For the steel cube projectile, the rebound of the steel cube projectile occurred when the impact velocity was less than 60 m/s for the sandwich carbon Miura foldcore and when the impact velocity was less than 50 m/s for the sandwich with the double layered Miura core (see Fig. 11 (g)). The ballistic limit for the carbon Miura foldcore type was 130 m/s (113 J) or more. The steel bar projectile with an impact energy of approximately 140 J was stuck in both the specimens. The sandwich structures with an aluminum Miura foldcore ( $H = 12$  mm,  $L = 6.28$  mm,  $S = V = 8.84$  mm,  $\rho = 0.02\rho_m$ , refer to Fig. 8 (a)) were impacted with a steel ball (mass: 110 g) [51], and a penetration of both the outer and inner face sheets occurred when the impact energy was 263 J or higher. Steel cubes (mass: 13.5 g), ice balls (mass: 23.63 g) and tire rubber (mass: 103 g) were also used in the high-velocity tests on sandwich structures with the aramid/phenolic Miura foldcore and CFRP skins [69,80]. Failures, such as a rebound from the outer skin, outer skin damage, core penetration, inner skin damage, and penetration were also observed (see Fig. 13 (b)). For the steel cube impact, the projectile rebounded from the outer skin when the impact energy was lower than 20 J. When the impact energy was low (20–40 J), the outer skin perforation occurred. In contrast, when the impact energy was high (45–80 J) (see Fig. 13 (b1)), the projectile was stuck in the foldcore, which absorbed the impact energy via the fracture and folding. For the steel bar impact, the outer skin and core penetration

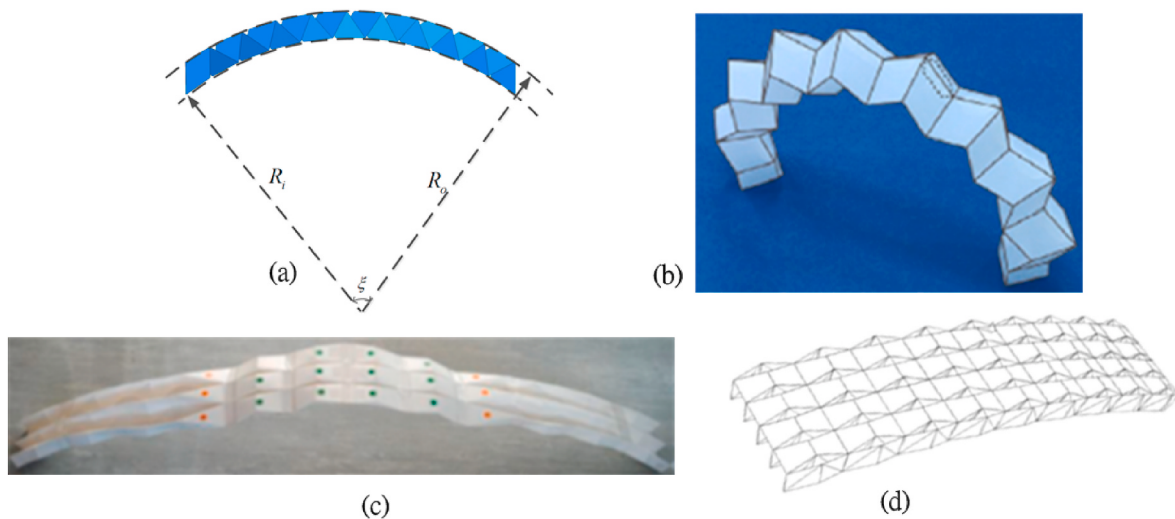


**Fig. 15.** Origami arcs. (a) Arc-Miura arch [88]; (b) double-kite arch [89]; (c) origami arch with a face switcher [44]; (d) interlocking origami arch [90].

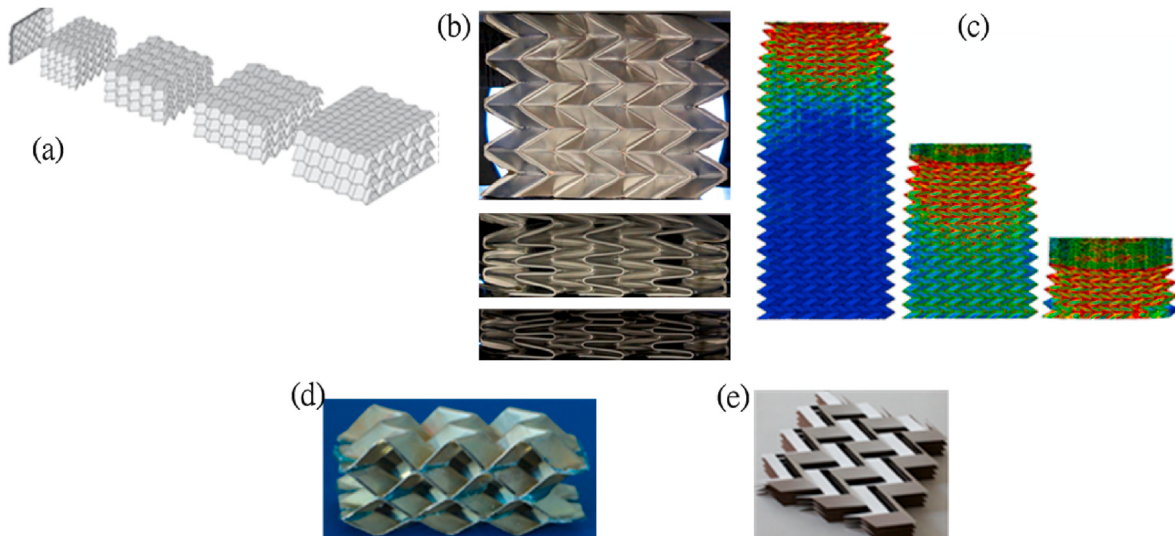


**Fig. 16.** Origami metamaterials. (a) Metamaterial obtained by stacking the sheets folded using the Miura pattern [92]; (b) quasi-static in-plane compression test on a Miura metamaterial [46]; (c) dynamic in-plane compression virtual test on a Miura metamaterial at  $V = 50$  m/s [104]; (d) multilayered metamaterial with a graded stiffness [105]; (e) zigzag-based folded material [107].

with the bar stopped by the inner skin occurred when the impact energy was higher than 78.7 J (see Fig. 13 (b2)). For the rubber beam projectile, no visible damage to the composite skins was noted even when the impact velocity reached 125.7 m/s, and the CT scan showed delamination of the outer skin and buckling damage to the foldcore (see Fig. 13 (b3)). The rubber projectile with a 90° shot angle was compressed in the axial direction on contact, followed by bending. Then it was straightened up and rebounded at a high velocity from the target, which caused delamination of the outer skin with little or no skin penetration, as well as the foldcore buckling/collapse. Besides, rubber projectile would spread out over the skin and the damage was typically over a wide area [80]. An FEA was also conducted for all the above-mentioned high-velocity impact tests, and it was proved to be a reliable computational method for predicting the crushing and impact damage [51,64,80, 84].

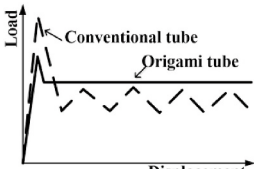
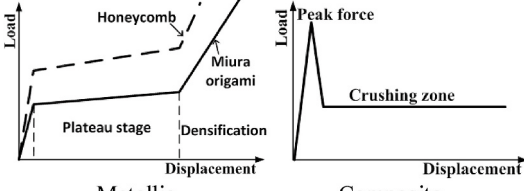
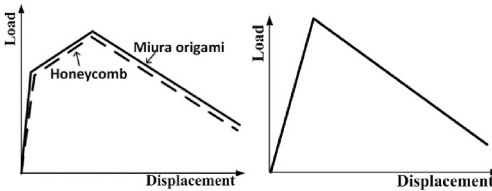
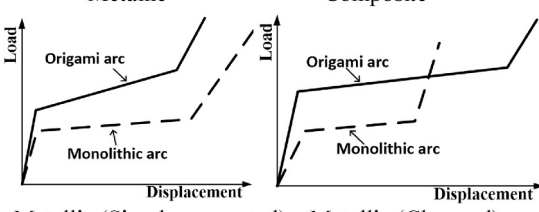
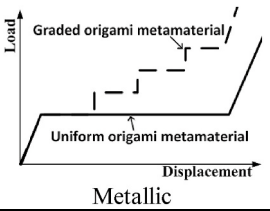
#### (c) Impulsive loading

Sandwich structures have been widely used for blast protection.

However, the shock resistant behaviors of the sandwich structures with a foldcore have not yet been widely investigated. The energy absorbing performance and maximum displacement of the structures are commonly assessed for structures under impulsive loading, and in general, the maximum displacement must be less than a critical value specified. The response of the Miura foldcore sandwich plates ( $a = 8.7\text{--}17.4$  mm,  $H = 10$  mm,  $\varphi = 29.14^\circ\text{--}74.03^\circ$ ,  $\theta = 17.39^\circ\text{--}40.51^\circ$ ; refer to Fig. 8 (a)) subjected to a high-intensity dynamic load representative of a blast was numerically studied using the ABAQUS/Explicit program [85]. It was found that in terms of the plastic energy dissipation, the alloy steel Miura foldcore outperformed the honeycomb core with the same material property and an equal area density by approximately 68% for low to moderate load intensities. A stacked folded core composed of several layers of different folded sheets with an ABABA stacking configuration (see Fig. 11 (h),  $S = L = H_A = 10$  mm,  $H_B = 25$  mm, where  $H_A$  and  $H_B$  are the heights of layers A and B, respectively; refer to Fig. 8 (a)) by using the Miura pattern was also proposed [79]. Depending on the different design parameters, the core either achieved a high peak force and subsequent strong softening or underwent a more uniform

**Table 2**

Summary of different origami structures.

Structure	Loading	Typical load-displacement curves	Remarks
Tube	Quasi-static lateral or axial		Origami tubes had a reduced initial peak and fluctuation and increased EA [20,21,45]
Foldcore	Quasi-static compression		Origami plates had a lower stiffness and strength compared with those of the corresponding honeycomb of the same area density under out-of-plane compression loading [48–51]
	Quasi-static shear or bending		Origami plates had a comparable or better stiffness and strength compared with those of the corresponding honeycomb of the same area density under in-plane shear loading [48–50]
Arc	Quasi-static compression		Simply supported: The origami arcs had a higher plateau force [88]; Clamped: The origami arcs had a longer stroke in the plateau stage and higher plateau force [88]
Metamaterial	Quasi-static compression		The graded structures had a larger EA efficiency (a multifold increase in the force) [105]

constant compressive strength. When subjected to impulsive loading, the compression collapse strength of the stacked folded core was as high as that of the honeycombs and foams having the same weight.

Overall, by designing the unit cell parameters, Miura-ori foldcores or their modified foldcores could achieve a wide range of mechanical behaviors, and therefore offer a rich design space to meet specified structural requirements.

#### 4. Origami arcs

Origami arcs can be formed from flat sheets by modifying the origami folding patterns [44]. A typical example is the arc-Miura foldcore (see Fig. 15 (a)) folded out of a Miura-derivative pattern [86]. The curved origami structures display significant flexibility in the overall shape, and they allow for large changes in the overall Gaussian curvature [87]. The arc-Miura specimens (inner arc radius  $R_i = 300$  mm, outer arc radius  $R_o = 330$  mm, arc rotation  $\xi = 70^\circ\text{--}154^\circ$ ) were compressed under an out-of-plane quasi-static load, and a parametric study was performed numerically [88]. It was shown that the SEA of the arc-Miura structure was two to four times that of the corresponding monolithic arch having the same radius of curvature and mass. You's research group proposed a series of origami arcs [44,89,90] (see Fig. 15 (b)–(d)). A new double-kite arch (see Fig. 15 (b)) was investigated experimentally and

numerically [89]. The results showed that the peak force was significantly dependent on the thickness of the crease lines; e.g., when the thickness of the crease line was reduced from 0.3 mm to 0.12 mm, the peak force reduced by 59%. The hinge rotation and face buckling were identified as the main failure mechanisms.

#### 5. Origami metamaterials

Metamaterials are human made materials that enable us to design atom like units and thereby create materials with the desired effective properties that are not available in nature [91]. The material properties are based on the microstructural geometry rather than the material composition of these materials. Origami-based metamaterials are realized by stacking of individual planar origami layers. In a stacked configuration, the origami pattern may vary from layer to layer. Origami-based metamaterials [92–98] are strong and lightweight [91], and have attracted considerable attention due to their special mechanical properties such as a negative Poisson's ratio [11,99–101] and designable stiffness [10,102,103]. Research on the EA performance of the origami metamaterials is mainly focused on several representative origami structures shown in Fig. 16, including the stacked Miura foldcores [92] and kirigami structures constructed from the Miura derivative patterns [93].

The individual folded Miura foldcores can be stacked and bonded along the joining creases to form a Miura metamaterial (see Fig. 16 (a)) [92]. Quasi-static in-plane compression tests were performed using the Miura-ori based metamaterials (see Fig. 16 (b),  $\varphi = 45^\circ/60^\circ$ ,  $\gamma = 60^\circ/100^\circ/148^\circ$ ,  $a = 10 \text{ mm}/20 \text{ mm}$ ,  $b = 10 \text{ mm}/20 \text{ mm}$ ; refer to Fig. 8 (a)), and it was found that the specimens with a large initial dihedral angle had a larger EA capacity per unit mass. It was also demonstrated that for the selected geometric parameters, the origami based metamaterials could outperform the honeycombs with the same relative density in terms of the SEA [46]. Dynamic in-plane compression tests were also conducted by the same research group (see Fig. 16 (c)) [104], on similar specimens with more unit cells in the loading direction by using the FEA method. Impact studies were performed considering uniform metamaterials ( $\varphi = 45^\circ$ ,  $\gamma = 60^\circ/100^\circ/148^\circ$ ,  $a = b = 10 \text{ mm}$ ; refer to Fig. 8 (a)) under a constant velocity impact ( $V = 50 \text{ m/s}$  or  $100 \text{ m/s}$ ). Uniform and graded metamaterials with a linearly varying cell wall thickness ( $\varphi = 45^\circ$ ,  $\gamma = 100^\circ$ ,  $a = b = 10 \text{ mm}$ ) were also investigated with an initial impact velocity of  $V_0$  ( $V_0 = 75 \text{ m/s}$  or  $125 \text{ m/s}$ ). The Miura-ori metamaterials exhibited an increased EA capacity with an increase in the loading rate, and a larger SEA was found in materials with larger initial dihedral angles.

A multilayered metamaterial with a periodically graded stiffness (see Fig. 16 (d)) when subjected to an out-of-plane quasi-static compression loading was demonstrated experimentally and numerically [105]. Altering the layer stacking order ( $\varphi$  order:  $42^\circ-54^\circ-50^\circ-46^\circ$ ,  $\gamma = 93.6^\circ$ ,  $a = 10.57 \text{ mm}$ ,  $b = 10 \text{ mm}$ , overall height =  $25.58 \text{ mm}$ ; refer to Fig. 8 (a)) could increase the SEA by up to 134.15% compared with that of a uniform metamaterial ( $\varphi$  order:  $48^\circ-48^\circ-48^\circ-48^\circ$ ). Uniform and graded Miura-ori Nylon metamaterials were compared by out-of-plane compression tests experimentally and numerically, and the result showed that the graded metamaterial could effectively avoid the force drop after the initial peak force and enhanced the EA capacity substantially [106].

Furthermore, a zigzag-based kirigami metamaterial folded by dislocating the zigzag strips of a Miura-ori crease pattern was proposed [107] (see Fig. 16 (e)). This metamaterial had the features of a low density and the realization of controllable deployable structures when compared with the corresponding Miura-ori pattern materials having the same geometrical parameters. However, the quasi-static, low-/high-velocity or impulsive loading tests have not yet been conducted on this type of metamaterial.

## 6. Concluding remarks

This article provides an overview on the energy absorption of origami structures. Existing research on origami thin-walled tubes, plates and sandwich structures with folded cores, origami arcs, and origami metamaterials under quasi-static loading, low/high-velocity impact or impulsive loading was discussed. The deformation modes, failure modes and energy absorbing capability of the structures under various loading conditions were reviewed. A summary of the simplified load-displacement relationships for the origami structures under different loadings or boundary conditions is presented in Table 2.

The existing research has clearly demonstrated that the energy absorbing capacity of the origami structures is closely linked to their geometries and the materials used to make these structures. Every single origami structure is associated with a particular geometrical pattern that enables it to be created out of a sheet material, and often, the geometrical parameters of these structures can be altered while preserving the foldability of the structures. This aspect enables us to design such structures. By choosing the geometry of the structure correctly and conscientiously, some origami structures can significantly outperform the conventional structures. For example, some of the origami thin-walled tubes reviewed in this article are superior to the conventional tubes because the prefolds not only trigger the deformation modes associated with a higher EA but also tend to reduce the  $F_{\max}$  and force

fluctuation, which is a highly desirable feature for crashworthiness cases. Most of the Miura foldcores show comparable or better mechanical performances than those of the corresponding honeycomb cores of the same density under quasi-static shear and bending loadings; however, an inferior performance is noted under compression. Clearly, more research is required to examine other origami units. Instead of simply picking a tessellation origami pattern and examining the EA performance of the folded structures, we should understand the behavior of the folds and their relationship with the failure modes. Doing so can enable us to properly design or at least identify the patterns that can induce the deformation modes with a higher EA capability.

The behavior of the origami structures and materials under dynamic loading warrants special attention. Current research focuses more on the quasi-static loads whereas studies on the dynamic effects have been rather limited. In addition, past research has shown that the graded materials are advantageous as energy absorbing structures under a dynamic loading [108–110]; however, relatively little effort has been expended to create origami graded structures although geometrically many origami patterns can be morphed together to form such structures.

Recently, the bio-origami structures [111,112] mimicked from natural folding structures such as insect's wing [111,113–115], leaves [111,112], durian shell [116] have been demonstrated a great potential for application to aerospace engineering, civil engineering. However, the EA characteristics of these bio-origami structures have not been fully understood. Meanwhile, a number of studies have suggested that bio-inspired structures exhibited superior EA capability compared with the conventional structures [117–119]. Moreover, Feng et al. [120] revealed that the bio-origami orthopyramid-like core panels is a promising structure for impact loading. Therefore, the investigation of bio-origami structures [111,112] in terms of EA is excellent for future directions.

We hope that this review will promote interest in novel origami structures and materials, especially with regard to their application as energy absorbing structures.

## Declaration of competing interest

The authors declare that they have no known competing financial interests or personal relationships that could have appeared to influence the work reported in this paper.

## Acknowledgements

Guoxing Lu would like to thank the Australian Research Council for financial support through Discovery Grants (DP160102612 and DP180102661). Zhong You gratefully acknowledges the support of the Air Force Office of Scientific Research (FA9550-16-1-0339).

## References

- [1] E.D. Demaine, J. O'Rourke, *Geometric Folding Algorithms: Linkages, Origami, Polyhedra*, Cambridge University Press, 2008.
- [2] A. Lebée, From folds to structures, a review, *Int. J. Space Struct.* 30 (2015) 55–74.
- [3] Z. You, Folding structures out of flat materials, *Science* 345 (2014) 623.
- [4] T. Nojima, K. Saito, Development of newly designed ultra-light core structures, *JSM Int. J. - Ser. A Solid Mech. Material Eng.* 49 (2006) 38–42.
- [5] N. Turner, B. Goodwine, M. Sen, A review of origami applications in mechanical engineering, *Proc. IME C J. Mech. Eng. Sci.* 230 (2015) 2345–2362.
- [6] K. Miura, Method of Packaging and Deployment of Large Membranes in Space, *The Institute of Space and Astronautical Science Report*, 1985, pp. 1–9.
- [7] S.J.P. Callens, A.A. Zadpoor, From flat sheets to curved geometries: origami and kirigami approaches, *Mater. Today* 21 (2018) 241–264.
- [8] A.P. Thrall, C.P. Quaglia, Accordion shelters: a historical review of origami-like deployable shelters developed by the US military, *Eng. Struct.* 59 (2014) 686–692.
- [9] C.P. Quaglia, A.J. Dascanio, A.P. Thrall, Bascule shelters: a novel erection strategy for origami-inspired deployable structures, *Eng. Struct.* 75 (2014) 276–287.
- [10] J.L. Silverberg, A.A. Evans, L. McLeod, R.C. Hayward, T. Hull, C.D. Santangelo, I. Cohen, Using origami design principles to fold reprogrammable mechanical metamaterials, *Science* 345 (2014) 647.

- [11] H. Yasuda, J. Yang, Reentrant origami-based metamaterials with negative Poisson's ratio and bistability, *Phys. Rev. Lett.* 114 (2015) 185502.
- [12] M. Thota, K.W. Wang, Tunable waveguiding in origami phononic structures, *J. Sound Vib.* 430 (2018) 93–100.
- [13] E. Boatti, N. Vassios, K. Bertoldi, Origami metamaterials for tunable thermal expansion, *Adv. Mater.* 29 (2017).
- [14] Y. Li, Z. You, Multi-corrugated indented foldcore sandwich panel for energy absorption, in: ASME 2015 International Design Engineering Technical Conferences and Computers and Information in Engineering Conference. Boston, Massachusetts, USA, 2015.
- [15] H. Buri, Y. Weinand, Origami - folded plate structures, architecture, in: 10th World Conference on Timber Engineering. Miyazaki, Japan, 2008.
- [16] G. Lu, T.X. Yu, *Energy Absorption of Structures and Materials*, first ed., Woodhead Publishing, Cambridge, 2003.
- [17] J.M. Alexander, An approximate analysis of the collapse of thin cylindrical shells under axial loading, *Q. J. Mech. Appl. Math.* 13 (1960) 10–15.
- [18] T. Nojima, Modelling of folding patterns in flat membranes and cylinders by origami, *JSME Int. J. - Ser. C* 45 (2002) 364–370.
- [19] J. Han, K. Yamazaki, S. Nishiyama, Optimization of the crushing characteristics of triangulated aluminum beverage cans, *Struct. Multidiscip. Optim.* 28 (2004) 47–54.
- [20] J. Song, Y. Chen, G. Lu, Axial crushing of thin-walled structures with origami patterns, *Thin-Walled Struct.* 54 (2012) 65–71.
- [21] J. Ma, Z. You, Energy absorption of thin-walled square tubes with a prefolded origami pattern-Part I: geometry and numerical simulation, *J. Appl. Mech.* 81 (2013), 011003.
- [22] D. Garrett, Z. You, J.M. Gattas, in: Curved Crease Tube Structures as an Energy Absorbing Crash Box. ASME 2016 International Design Engineering Technical Conferences and Computers and Information in Engineering Conference. Charlotte, North Carolina, 2016.
- [23] J. Ma, D. Hou, Y. Chen, Z. You, Quasi-static axial crushing of thin-walled tubes with a kite-shape rigid origami pattern: numerical simulation, *Thin-Walled Struct.* 100 (2016) 38–47.
- [24] B. Wang, C. Zhou, The imperfection-sensitivity of origami crash boxes, *Int. J. Mech. Sci.* 121 (2017) 58–66.
- [25] C. Zhou, Y. Zhou, B. Wang, Crashworthiness design for trapezoid origami crash boxes, *Thin-Walled Struct.* 117 (2017) 257–267.
- [26] K. Yang, S. Xu, J. Shen, S. Zhou, Y.M. Xie, Energy absorption of thin-walled tubes with pre-folded origami patterns: numerical simulation and experimental verification, *Thin-Walled Struct.* 103 (2016) 33–44.
- [27] K. Yang, S. Xu, S. Zhou, Y.M. Xie, Multi-objective optimization of multi-cell tubes with origami patterns for energy absorption, *Thin-Walled Struct.* 123 (2018) 100–113.
- [28] P. Christy Albert, A. Radzi Ab Ghani, M. Zaid Othman, A.M. Ahmad Zaidi, Axial crushing behavior of aluminum square tube with origami pattern, *Mod. Appl. Sci.* 10 (2016) 90.
- [29] N.S. Ha, G. Lu, X. Xiang, High energy absorption efficiency of thin-walled conical corrugation tubes mimicking coconut tree configuration, *Int. J. Mech. Sci.* 148 (2018) 409–421.
- [30] H. Yasuda, T. Yein, T. Tachi, K. Miura, M. Taya, Folding behaviour of Tachi-Miura polyhedron bellows, *Proc. Math. Phys. Eng. Sci.* 469 (2013) 20130351.
- [31] J. Cai, X. Deng, J. Feng, Y. Zhou, Geometric design and mechanical behavior of a deployable cylinder with Miura origami, *Smart Mater. Struct.* 24 (2015) 125031.
- [32] S. Ming, Z. Song, T. Li, K. Du, C. Zhou, B. Wang, The energy absorption of thin-walled tubes designed by origami approach applied to the ends, *Mater. Des.* 192 (2020) 108725.
- [33] H. Ye, J. Ma, X. Zhou, H. Wang, Z. You, Energy absorption behaviors of pre-folded composite tubes with the full-diamond origami patterns, *Compos. Struct.* 221 (2019) 110904.
- [34] C. Zhou, B. Wang, J. Ma, Z. You, Dynamic axial crushing of origami crash boxes, *Int. J. Mech. Sci.* 118 (2016) 1–12.
- [35] S. Ming, C. Zhou, T. Li, Z. Song, B. Wang, Energy absorption of thin-walled square tubes designed by kirigami approach, *Int. J. Mech. Sci.* 157–158 (2019) 150–164.
- [36] H. Wang, C. Guo, Y. Li, Y. Liu, M. Wang, Z. You, D. Zhao, Structural design and forming method of single-curved surface structure based on Miura-origami, in: ASME 2016 International Design Engineering Technical Conferences and Computers and Information in Engineering Conference. Charlotte, North Carolina, 2016.
- [37] T.-U. Lee, X. Yang, J. Ma, Y. Chen, J.M. Gattas, Elastic buckling shape control of thin-walled cylinder using pre-embedded curved-crease origami patterns, *Int. J. Mech. Sci.* 151 (2019) 322–330.
- [38] M.O.W. Richardson, M.J. Wisheart, Review of low-velocity impact properties of composite materials, *Compos. Appl. Sci. Manuf.* 27 (1996) 1123–1131.
- [39] C. Zhou, L. Jiang, K. Tian, X. Bi, B. Wang, Origami crash boxes subjected to dynamic oblique loading, *J. Appl. Mech.* 84 (2017), 091006.
- [40] T.H. Kim, S.R. Reid, Multiaxial softening hinge model for tubular vehicle roll-over protective structures, *Int. J. Mech. Sci.* 43 (2001) 2147–2170.
- [41] Aasho-Agc-ARTBA Joint Cooperation Committee, Subcommittee on New Highway Materials, Task Force No. 13, Officials AAoSHaT. A Guide to Standardized Highway Barrier Hardware, American Association of State Highway and Transportation Officials, 1995.
- [42] Y.-Y. Jing, D.C. Barton, The response of square cross-section tubes under lateral impact loading, *Int. J. Crashworthiness* 3 (1998) 359–378.
- [43] D. Kecman, Bending collapse of rectangular and square section tubes, *Int. J. Mech. Sci.* 25 (1983) 623–636.
- [44] Y. Li, *Thin-walled Structures for Energy Absorption* (Ph.D thesis), University of Oxford, 2016.
- [45] J. Ma, Z. You, Energy absorption of thin-walled beams with a pre-folded origami pattern, *Thin-Walled Struct.* 73 (2013) 198–206.
- [46] J. Zhang, D. Karagiozova, Z. You, Y. Chen, G. Lu, Quasi-static large deformation compressive behaviour of origami-based metamaterials, *Int. J. Mech. Sci.* 153–154 (2019) 194–207.
- [47] Y. Lv, Y. Zhang, N. Gong, Z.-x Li, G. Lu, X. Xiang, On the out-of-plane compression of a Miura-ori patterned sheet, *Int. J. Mech. Sci.* 161–162 (2019) 105022.
- [48] X. Zhou, H. Wang, Z. You, Mechanical properties of Miura-based folded cores under quasi-static loads, *Thin-Walled Struct.* 82 (2014) 296–310.
- [49] M. Grzeschik, Performance of foldcores mechanical properties and testing, in: ASME 2013 International Design Engineering Technical Conferences and Computers and Information in Engineering Conference. Portland, Oregon, USA, 2013.
- [50] S. Fischer, Realistic FE simulation of foldcore sandwich structures, *Int. J. Mech. Mater. Eng.* 10 (2015).
- [51] S. Fischer, Aluminium foldcores for sandwich structure application: mechanical properties and FE-simulation, *Thin-Walled Struct.* 90 (2015) 31–41.
- [52] J.M. Gattas, Z. You, Quasi-static impact of indented foldcores, *Int. J. Impact Eng.* 73 (2014) 15–29.
- [53] M. Grzeschik, Y. Klett, P. Middendorf, Reality check - mechanical potential of tessellation-based foldcore materials, in: 7th International Meeting on Origami in Science, Mathematics, and Education, Oxford University, 2018, pp. 1273–1284.
- [54] M. Klaus, H.G. Reimerdes, N.K. Gupta, Experimental and numerical investigations of residual strength after impact of sandwich panels, *Int. J. Impact Eng.* 44 (2012) 50–58.
- [55] S. Heimbs, P. Middendorf, S. Kilchert, A.F. Johnson, M. Maier, Experimental and numerical analysis of composite folded sandwich core structures under compression, *Appl. Compos. Mater.* 14 (2008) 363–377.
- [56] S. Fischer, K. Drechsler, S. Kilchert, A. Johnson, Mechanical tests for foldcore base material properties, *Compos. Appl. Sci. Manuf.* 40 (2009) 1941–1952.
- [57] K. Jiang, K. Cai, M. Wang, D. Zhao, Z. You, Experimental study of manufacture and mechanical behavior of sandwich structure with composite foldcores, in: ASME 2015 International Design Engineering Technical Conferences and Computers and Information in Engineering Conference. Boston, Massachusetts, USA, 2015.
- [58] S. Liu, G. Lu, Y. Chen, Y.W. Leong, Deformation of the Miura-ori patterned sheet, *Int. J. Mech. Sci.* 99 (2015) 130–142.
- [59] Y. Hao, S. Zang, H. Wang, Z. You, X. Zhou, Virtual testing of foldcores made of polyethylene terephthalate, in: 20th International Conference on Composite Materials. Copenhagen, 2015.
- [60] Z. Chen, T. Wu, G. Nian, Y. Shan, X. Liang, H. Jiang, S. Qu, Ron Resch origami pattern inspired energy absorption structures, *J. Appl. Mech.* 86 (2019).
- [61] S. Zang, X. Zhou, H. Wang, Z. You, Foldcores made of thermoplastic materials: experimental study and finite element analysis, *Thin-Walled Struct.* 100 (2016) 170–179.
- [62] S. Heimbs, Foldcore sandwich structures and their impact behaviour: an overview, in: S. Abrate, B. Castañé, R. YDS (Eds.), *Solid Mechanics and its Applications*, Springer, The Netherlands, 2013, pp. 491–544.
- [63] R. Sturm, S. Fischer, Virtual design method for controlled failure in foldcore sandwich panels, *Appl. Compos. Mater.* 22 (2015) 791–803.
- [64] S. Heimbs, J. Cichosz, M. Klaus, S. Kilchert, A.F. Johnson, Sandwich structures with textile-reinforced composite foldcores under impact loads, *Compos. Struct.* 92 (2010) 1485–1497.
- [65] S. Heimbs, P. Middendorf, C. Hampf, F. Hänel, K. Wolf, Aircraft sandwich structures with folded core under impact load, in: 8th International Conference on Sandwich Structures (ICSS-8). Porto, 2008, pp. 369–380.
- [66] S. Heimbs, Virtual testing of sandwich core structures using dynamic finite element simulations, *Comput. Mater. Sci.* 45 (2009) 205–216.
- [67] S. Kilchert, A.F. Johnson, H. Voggenreiter, Modelling the impact behaviour of sandwich structures with folded composite cores, *Compos. Appl. Sci. Manuf.* 57 (2014) 16–26.
- [68] S. Kilchert, A. Johnson, A. Reiter, R. Jemmali, Gas gun impact tests on improved sandwich panels, in: Cellular structures for impact performance, Sixth Framework Programme FP6-2005-Aero-1, 2008.
- [69] N. Toso-Pentecote, A. Johnson, Impact damage in sandwich composite structures from gas gun tests, in: E.E. Gdoutos (Ed.), *Experimental Analysis of Nano and Engineering Materials and Structures*, Springer Netherlands, Dordrecht, 2007, pp. 771–772.
- [70] M.R.M. Rejab, W.J. Cantwell, The mechanical behaviour of corrugated-core sandwich panels, *Compos. B Eng.* 47 (2013) 267–277.
- [71] L.X. Cong, Y.G. Sun, Compression response of sandwich structure with M-Type CFRP foldcore, *Adv. Mater. Res.* 1049–1050 (2014) 1071–1074.
- [72] D.P.T. Minh, Numerical simulation for the folded core sandwich plates under torsion by homogenization method, *Am. J. Eng. Res.* 6 (2017) 149–155.
- [73] L. Cong, Y. Sun, X. Wang, Bending response of foldcore composite sandwich beams, *Comput. Mater. Continua (CMC)* 47 (2015) 1–14.
- [74] X.M. Xiang, Z. You, G. Lu, Rectangular sandwich plates with Miura-ori folded core under quasi-static loadings, *Compos. Struct.* 195 (2018) 359–374.
- [75] M. Kintscher, L. Kärger, A. Wetzel, D. Hartung, Stiffness and failure behaviour of folded sandwich cores under combined transverse shear and compression, *Compos. Appl. Sci. Manuf.* 38 (2007) 1288–1295.
- [76] R. Sturm, Y. Klett, C. Kindervater, H. Voggenreiter, Failure of CFRP airframe sandwich panels under crash-relevant loading conditions, *Compos. Struct.* 112 (2014) 11–21.

- [77] T.N. Cash, H.S. Warren, J.M. Gattas, Analysis of Miura-type folded and morphing sandwich beams, in: ASME 2015 International Design Engineering Technical Conferences and Computers and Information in Engineering Conference. Boston, Massachusetts, USA, 2015.
- [78] J.M. Gattas, Z. You, Quasi-static impact response of single-curved foldcore sandwich shells, in: ASME 2014 International Design Engineering Technical Conferences and Computers and Information in Engineering Conference. Buffalo, New York, USA, 2014.
- [79] M. Schenk, S.D. Guest, G.J. McShane, Novel stacked folded cores for blast-resistant sandwich beams, *Int. J. Solid Struct.* 51 (2014) 4196–4214.
- [80] A. Johnson, S. Kilchert, S. Fischer, N. Toso-Pentecôte, Design and performance of novel aircraft structures with folded composite cores, in: Structural Integrity and Durability of Advanced Composites, 2015, pp. 793–827.
- [81] W. He, J. Liu, S. Wang, D. Xie, Low-velocity impact response and post-impact flexural behaviour of composite sandwich structures with corrugated cores, *Compos. Struct.* 189 (2018) 37–53.
- [82] M. Klaus, H. Reimerdes, Residual strength simulations of sandwich panels after impact, in: 17th International Conference on Composite Materials (ICCM-17). Edinburgh, 2009.
- [83] Z. Feng, L. Guoxing, R. Dong, W. Zhihua, Plastic deformation, failure and energy absorption of sandwich structures with metallic cellular cores, *Int. J. Prot. Struct.* 1 (2010) 507–541.
- [84] A.F. Johnson, N. Toso-Pentecôte, S. Kilchert, Validation of damage modelling in composite fuselage structures under high velocity impact, *CEAS Aeronaut. J.* 4 (2013) 253–264.
- [85] A. Pydah, R.C. Batra, Crush dynamics and transient deformations of elastic-plastic Miura-ori core sandwich plates, *Thin-Walled Struct.* 115 (2017) 311–322.
- [86] J.M. Gattas, W. Wu, Z. You, Miura-base rigid origami: parameterizations of first-level derivative and piecewise geometries, *J. Mech. Des.* 135 (2013) 111011.
- [87] A.D. Norman, K.A. Seffen, S.D. Guest, Morphing of curved corrugated shells, *Int. J. Solid Struct.* 46 (2009) 1624–1633.
- [88] X.M. Xiang, G. Lu, D. Ruan, Z. You, M. Zolghadr, Large deformation of an arc-Miura structure under quasi-static load, *Compos. Struct.* 182 (2017) 209–222.
- [89] J.M. Gattas, W. Lv, Y. Chen, Rigid-foldable tubular arches, *Eng. Struct.* 145 (2017) 246–253.
- [90] Y. Li, Z. You, Thin-walled open-section origami beams for energy absorption, in: ASME 2014 International Design Engineering Technical Conferences and Computers and Information in Engineering Conference. Buffalo, New York, USA, 2014.
- [91] X. Yu, J. Zhou, H. Liang, Z. Jiang, L. Wu, Mechanical metamaterials associated with stiffness, rigidity and compressibility: a brief review, *Prog. Mater. Sci.* 94 (2018) 114–173.
- [92] M. Schenk, S.D. Guest, Geometry of miura-folded metamaterials, *Proc. Natl. Acad. Sci. U. S. A.* 110 (2013) 3276–3281.
- [93] M. Eidini, G.H. Paulino, Unraveling metamaterial properties in zigzag-base folded sheets, *Sci. Adv.* 1 (2015).
- [94] T. Tachi, Designing freeform origami tessellations by generalizing resch's patterns, *J. Mech. Des.* 135 (2013) 111006.
- [95] J.L. Silverberg, J.-H. Na, A.A. Evans, B. Liu, T.C. Hull, D. Santangelo Christian, R. J. Lang, R.C. Hayward, I. Cohen, Origami structures with a critical transition to bistability arising from hidden degrees of freedom, *Nat. Mater.* 14 (2015) 389.
- [96] T. Al-Mulla, M.J. Buehler, Folding creases through bending, *Nat. Mater.* 14 (2015) 366.
- [97] T. Tachi, K. Miura, Rigid-foldable cylinders and cells, *J. Int. Assoc. Shell Spatial Struct.* 53 (2012) 217–226.
- [98] J.T. Overvelde, T.A. de Jong, Y. Shevchenko, S.A. Becerra, G.M. Whitesides, J. C. Weaver, C. Hoberman, K. Bertoldi, A three-dimensional actuated origami-inspired transformable metamaterial with multiple degrees of freedom, *Nat. Commun.* 7 (2016) 10929.
- [99] Z.Y. Wei, Z.V. Guo, L. Dudte, H.Y. Liang, L. Mahadevan, Geometric mechanics of periodic pleated origami, *Phys. Rev. Lett.* 110 (2013) 215501.
- [100] X. Zhou, S. Zang, Z. You, Origami mechanical metamaterials based on the miura-derivative fold patterns, *Proc R Soc A Math Phys Eng Sci* 472 (2016).
- [101] S. Kamrava, D. Mousanezhad, H. Ebrahimi, R. Ghosh, A. Vaziri, Origami-based cellular metamaterial with auxetic, bistable, and self-locking properties, *Sci. Rep.* 7 (2017) 46046.
- [102] K. Virk, A. Monti, T. Trehard, M. Marsh, K. Hazra, K. Boba, C.D.L. Remillat, F. Scarpa, I.R. Farrow, SILICOMB PEEK Kirigami cellular structures: mechanical response and energy dissipation through zero and negative stiffness, *Smart Mater. Struct.* 22 (2013), 084014.
- [103] E.T. Filipov, T. Tachi, G.H. Paulino, Origami tubes assembled into stiff, yet reconfigurable structures and metamaterials, *Proc. Natl. Acad. Sci. Unit. States Am.* 112 (2015) 12321.
- [104] D. Karagiozova, J. Zhang, G. Lu, Z. You, Dynamic in-plane compression of Miura-ori patterned metamaterials, *Int. J. Impact Eng.* 129 (2019) 80–100.
- [105] J. Ma, J. Song, Y. Chen, An origami-inspired structure with graded stiffness, *Int. J. Mech. Sci.* 136 (2018) 134–142.
- [106] X. Xiang, W. Qiang, B. Hou, P. Tran, G. Lu, Quasi-static and dynamic mechanical properties of Miura-ori metamaterials, *Thin-Walled Struct.* 157 (2020) 106993.
- [107] M. Eidini, Zigzag-base folded sheet cellular mechanical metamaterials, *Extreme Mech. Lett.* 6 (2016) 96–102.
- [108] C.J. Shen, G. Lu, T.X. Yu, Dynamic behavior of graded honeycombs – a finite element study, *Compos. Struct.* 98 (2013) 282–293.
- [109] C.J. Shen, T.X. Yu, G. Lu, Double shock mode in graded cellular rod under impact, *Int. J. Solid Struct.* 50 (2013) 217–233.
- [110] C.J. Shen, G. Lu, D. Ruan, T.X. Yu, Propagation of the compaction waves in a cellular block with varying cross-section, *Int. J. Solid Struct.* 88–89 (2016) 319–336.
- [111] L. Mahadevan, S. Rica, Self-organized origami, *Science* 307 (2005) 1740.
- [112] D. Baerlecken, M. Swarts, R. Gentry, N. Wonoto, Bio-origami: Form Finding and Evaluation of Origami Structures, 2012.
- [113] N. Ha, T. Jin, N. Goo, H. Park, Anisotropy and non-homogeneity of an Allomyrina Dichotoma beetle hind wing membrane, *Bioinspiration Biomimetics* 6 (2011), 046003.
- [114] N.S. Ha, Q.T. Truong, N.S. Goo, H.C. Park, Biomechanical properties of insect wings: the stress stiffening effects on the asymmetric bending of the allomyrina dichotoma beetle's hind wing, *PLoS One* 8 (2013), e80689.
- [115] N.S. Ha, Q.T. Truong, N.S. Goo, H.C. Park, Relationship between wingbeat frequency and resonant frequency of the wing in insects, *Bioinspiration Biomimetics* 8 (2013), 046008.
- [116] N.S. Ha, G. Lu, D. Shu, T.X. Yu, Mechanical properties and energy absorption characteristics of tropical fruit durian (*Durio zibethinus*), *J. Mech. Behav. Biomed. Mater.* 104 (2020) 103603.
- [117] N.S. Ha, G. Lu, X. Xiang, Energy absorption of a bio-inspired honeycomb sandwich panel, *J. Mater. Sci.* 54 (2019) 6286–6300.
- [118] X. Xiang, S. Zou, N.S. Ha, G. Lu, I. Kong, Energy absorption of bio-inspired multi-layered graded foam-filled structures under axial crushing, *Compos. B Eng.* 198 (2020) 108216.
- [119] N.S. Ha, G. Lu, A review of recent research on bio-inspired structures and materials for energy absorption applications, *Compos. B Eng.* (2019) 107496.
- [120] Y. Feng, K. Li, Y. Gao, H. Qiu, J. Liu, Design and optimization of origami-inspired orthopyramid-like core panel for load damping, *Appl. Sci.* 9 (2019) 4619.